

This is a repository copy of *Terrain analysis using radar shape-from-shading*.

White Rose Research Online URL for this paper:

<https://eprints.whiterose.ac.uk/945/>

Article:

Bors, A G orcid.org/0000-0001-7838-0021, Hancock, E R orcid.org/0000-0003-4496-2028 and Wilson, R C orcid.org/0000-0001-7265-3033 (2003) Terrain analysis using radar shape-from-shading. IEEE Transactions on Pattern Analysis and Machine Intelligence. pp. 974-992. ISSN 0162-8828

<https://doi.org/10.1109/TPAMI.2003.1217602>

Reuse

Items deposited in White Rose Research Online are protected by copyright, with all rights reserved unless indicated otherwise. They may be downloaded and/or printed for private study, or other acts as permitted by national copyright laws. The publisher or other rights holders may allow further reproduction and re-use of the full text version. This is indicated by the licence information on the White Rose Research Online record for the item.

Takedown

If you consider content in White Rose Research Online to be in breach of UK law, please notify us by emailing eprints@whiterose.ac.uk including the URL of the record and the reason for the withdrawal request.

Terrain Analysis Using Radar Shape-from-Shading

Adrian G. Bors, *Member, IEEE*, Edwin R. Hancock, and
Richard C. Wilson, *Member, IEEE Computer Society*

Abstract—This paper develops a maximum a posteriori (MAP) probability estimation framework for shape-from-shading (SFS) from synthetic aperture radar (SAR) images. The aim is to use this method to reconstruct surface topography from a single radar image of relatively complex terrain. Our MAP framework makes explicit how the recovery of local surface orientation depends on the whereabouts of terrain edge features and the available radar reflectance information. To apply the resulting process to real world radar data, we require probabilistic models for the appearance of terrain features and the relationship between the orientation of surface normals and the radar reflectance. We show that the SAR data can be modeled using a Rayleigh-Bessel distribution and use this distribution to develop a maximum likelihood algorithm for detecting and labeling terrain edge features. Moreover, we show how robust statistics can be used to estimate the characteristic parameters of this distribution. We also develop an empirical model for the SAR reflectance function. Using the reflectance model, we perform Lambertian correction so that a conventional SFS algorithm can be applied to the radar data. The initial surface normal direction is constrained to point in the direction of the nearest ridge or ravine feature. Each surface normal must fall within a conical envelope whose axis is in the direction of the radar illuminant. The extent of the envelope depends on the corrected radar reflectance and the variance of the radar signal statistics. We explore various ways of smoothing the field of surface normals using robust statistics. Finally, we show how to reconstruct the terrain surface from the smoothed field of surface normal vectors. The proposed algorithm is applied to various SAR data sets containing relatively complex terrain structure.

Index Terms—Synthetic aperture radar imaging, shape-from-shading, terrain surface reconstruction, maximum a posteriori probability estimation, robust statistics.

1 INTRODUCTION

RECOVERING terrain topography from synthetic aperture radar (SAR) images. It was the need to develop techniques for mapping the surface of planet Venus from Magellan imagery that has stimulated research in the area [1]. Due to the nature of the radar image acquisition process, the task of interpreting SAR images poses a number of challenges. Such problems are caused by the complex physics of radiation-material interaction, the radar beam, wavelength, variations due to the vegetation, level of humidity, type of terrain, foreshortening, layover, shadowing, man-made objects, or the process of radar image acquisition [2], [3], [4], [5], [6], [7], [8], [9], [10]. The study of terrain SAR images is termed radarclinometry and has been shown to provide a powerful means of probing three-dimensional structure [9], [11], [12], [13], [14], [15], [16], [17]. Although there are a number of well-developed methods for recovering three-dimensional surface structure from multiple radar images, there is relatively little work aimed at terrain analysis from single SAR images. In the computer vision literature, the pioneering work on the subject was performed by Frankot and Chellappa [11], who extended the Lambertian shape-from-shading method of Ikeuchi and Horn [18] to radar reflectance. One of the important features of the method was the way in which it imposed integrability constraints on surface reconstruction in the Fourier domain.

Despite the significant effort in the area, one of the shortcomings of existing work is its lack of a statistical basis. This is an important omission since radar data is notoriously noisy. Hence, the aim in this paper is to develop a statistical framework for radar shape-from-shading. Specifically, we develop a maximum a posteriori probabilistic framework, which allows surface normals to be estimated using a model of the radar reflectance function and an estimate of the whereabouts to ridge and ravine structures in the terrain under study. In the remainder of this section, we review the related literature in more detail and outline the main novelty of our contribution.

1.1 Related Literature

One of the classical approaches to SFS was the regularization method introduced by Ikeuchi and Horn [18] and later extended and developed by Horn and Brooks [19]. According to the regularization framework, the field of surface normals is iteratively updated so as to minimize a brightness error subject to local smoothness constraints. The main limitation of this approach is the need to balance the effects of brightness and smoothness errors while adjusting the surface normal directions. Specifically, it has a marked tendency to over-smooth the surface normals and erode fine surface detail. Recently, Worthington and Hancock [20] have attempted to remedy this problem by imposing the image irradiance equation as a hard constraint. According to their approach, the surface normals are constrained to always lie on a cone whose apex angle is determined by the image brightness and whose axis is in the light source direction. There are many alternative approaches to SFS, including Oliensis and Dupuis [21] algorithm of steepest descent from singular points and the use of level sets algorithms [22]. An extensive review and

• The authors are with the Department of Computer Science, University of York, York YO10 5DD, UK.
E-mail: {Adrian.Bors, erh, wilson}@cs.york.ac.uk.

Manuscript received 22 Mar. 2002; revised 24 Oct. 2002; accepted 28 Oct. 2002.
Recommended for acceptance by J. Beveridge.
For information on obtaining reprints of this article, please send e-mail to: tpami@computer.org, and reference IEEECS Log Number 116136.

comparative study of these and related methods is contained in the paper of Zhang et al. [23].

The application of shape-from-shading to radar imagery has also attracted considerable interest. Guindon [12] has shown that the main sources of error in SFS for SAR images are foreshortening, layover, and image noise. Foreshortening, i.e., the effect caused in the radar returns by steep surface inclination and layover, i.e., the superposition of multiple radar returns, both result in locally enhanced brightness and are, hence, difficult to model. Multiple scattering also results in an increase in the radar signal variance, which further complicates the analysis of SAR reflectance [2], [3], [8], [9], [16]. Frankot and Chellappa [11] have extracted empirical reflectance models from SAR images using an exhaustive parameter search method. Their model is used in conjunction with a modified version of the regularized SFS method of Horn and Brooks [19]. This method uses a surface integrability algorithm based on the Discrete Fourier Transform. More recently, Fua has shown how snake energy functions can be used to fit a 3D surface model to height data derived from radar SFS [13]. Paquerault et al. [24] show how Markov Random Fields can be used to recover the height contour map using a terrain reflectance model. Meanwhile, Chorowicz et al. [25] have developed a method for recognizing relief patterns in filtered SAR images using syntactic analysis. A shape-from-shading algorithm, which imports techniques from differential geometry, fluid dynamics, and numerical analysis was proposed by Kimmel et al. [26]. Ostrov [16] adopts a variational approach which involves solving the time-dependent Hamilton-Jacobi equation under boundary constraints to reconstruct terrain shape.

The majority of SFS studies in the photometric domain use a Lambertian reflectance model [19], [20], [27] which assumes that the observed image brightness is proportional to the cosine of the local angle of illuminant incidence. Unfortunately, due to the statistical and reflectivity properties of SAR images, Lambertian models are not directly applicable [11], [13], [16]. Various statistical approaches have been used to model the distribution of SAR image statistics. In particular, Gamma [15], [28], [29], [30], Rayleigh [31], [32], and Gaussian [6], [7], [11], [33] distributions have proven effective for a variety of SAR image analysis tasks. There have been several attempts to parametrically model the radar reflectance function for SAR images [11], [12]. The main obstacle to the use of these methods is that the reflectance function parameters depend on the radar image acquisition conditions and are, hence, difficult to estimate.

In radar shape-from-shading, as with conventional shape-from-shading, boundary constraints can be used to initialize the directions of the estimated field of surface normals. In terrain analysis, the constraints can be provided by the whereabouts of various topographical features such as ridges and ravines. However, the detection of features in radar imagery is itself a challenging problem. The reason for this is that the dominant noise process in radar images is speckle. As concrete examples, both Bovik [28] and Touzi et al. [34] have used ratio-of-averages edge detectors for feature detection in speckle images. Oliver et al. have shown that this edge detector is optimal when the SAR image statistics follow a Gamma distribution [29]. Other edge detectors for SAR images have been proposed by Caves et al. [15] and by Beauchemin et al. [35]. Additionally, filtering followed by classical edge detection has been attempted in SAR images [25], [30], [33], [36]. However, filtering distorts the characteristic image distribution and useful information is lost. A

better approach is to find a maximum likelihood estimator for the specific image distribution model. A Bayes method for estimating the noise and despeckling SAR images based on Gibbs random fields was proposed by Datcu et al. [37]. Both Evans et al. [33] and Czerwinski et al. [36] have used a product of Rayleigh and Bessel function distributions as a SAR image model. In the former case, line-features are detected using probabilistic relaxation, while line orientation is selected by hypothesis testing in the latter.

1.2 Contribution

As noted above, although there has been considerable work aimed at recovering terrain structure using radar shape-from-shading, the statistical methodology for this task has remained rather limited. The aim in this paper is therefore to develop a MAP estimation framework for radar shape-from-shading and to develop statistical models of the underlying image statistics and radar reflectivity.

We commence by constructing a model of the SAR image statistics. Specifically, we derive a more general distribution than those used previously, which is a product of Rayleigh and Bessel functions. The Gamma and Rayleigh models employed in some previous approaches are particular cases of the proposed distribution. Robust estimators are used to recover the parameters of the distribution. Our model for the SAR image reflectivity function is an empirical one which is obtained using information provided by a ground-truth digital elevation map (DEM). We use the inverse reflectivity function to transform the raw radar data so that we can perform Lambertian shape-from-shading on it.

Once the SAR image model and the characteristic reflectivity function are to hand, then we can proceed with terrain analysis using SFS. We adopt a maximum a posteriori probability (MAP) criterion to recover the field of surface normals. The probability density functions which underpin this method are represented using simple energy functions [38]. There are two energy terms. The first of these is a data-closeness term that represents the compliance of the recovered surface normals with the radar reflectance equation and also with directional constraints provided by the whereabouts of salient topographical terrain features. The second term models the smoothness of the recovered field of surface normals.

Turning our attention to the first of these energy terms, according to our MAP estimation method, the orientation of the surface normals depends on the SAR image model as well as on the boundary constraints imposed by the whereabouts of topographic features. In order to locate the topographic features, we develop a maximum likelihood edge detector using the Rayleigh-Bessel model. We constrain the recovery of surface normals by considering the nature of the detected features in the SAR image. In this sense, we classify the detected features into those corresponding to ridges and those corresponding to ravines. Ridges are the peaks of structures of convex terrain topography, while ravines correspond to bottoms of concave terrain topography. Ridges correspond to sources of divergent vector fields, whereas ravines are the sinks of convergent vector fields. We provide a simple statistical test which allows us to distinguish between these two topographical alternatives.

The second energy term models the smoothing of the vector field. We explore the use of a number of alternative robust statistical estimators for smoothing the field of surface normals [39]. These include the marginal median [40], [41] and the vector median [42].

Once the smoothed field of surface normals is to hand, then we can reconstruct the surface height map. To do this, we use a simple method employing two steps [43]. In the first step, we choose the location of the site that we will update, while, in the second step, we do the updating using the height from a known reference. We compare the results obtained with our new method for radar shape-from-shading with those reported by Zheng and Chellappa [23], [27] and by Bichsel and Pentland [23], [44].

Radar shape-from-shading is a complex problem for which “the devil is in the detail.” Hence, the contribution of this paper is to bring together a number of existing and new ideas, which each go some way to extending the methodology for radar shape-from-shading.

The outline of this paper is as follows: In Section 2, we introduce a maximum a posteriori approach for SFS. In Section 3.1, we present the SAR image model and, in Section 3.2, we show how to estimate the model parameters. Section 3.3 describes how we derive the SAR reflectivity function using ground-truth DEM data. In Section 4, we derive the optimal edge detector for the Rayleigh-Bessel distribution. The algorithm proposed for recovering the 3D surface is described in Section 5. Section 5.1 provides details of how we initialize the smoothing algorithm. The needle-map smoothing algorithms are outlined in Section 5.2, while, in Section 5.3, we outline a method for estimating the 3D height information from the smoothed vector field of surface normals. Section 6 presents the experimental results obtained when the proposed SFS method is applied to SAR images of terrain. Finally, Section 7 draws some conclusions from the present study and suggests directions for future investigation.

2 A MAXIMUM A POSTERIORI APPROACH FOR SHAPE-FROM-SHADING

Probabilistic models have proven to be highly effective in many areas of pattern recognition and computer vision [37], [38], [45]. In this paper, we propose a maximum a posteriori criterion for shape-from-shading. The shape-from-shading problem can be posed as the recovery of vector-field of surface normals from 2D image data using boundary constraints provided by edges or other topographic features. Let us denote by $P(\mathcal{V}, \mathcal{E}|I_{3D}, I_{2D})$ the a posteriori probability of jointly recovering the field of surface normals \mathcal{V} and the edge map \mathcal{E} from the 3D shape denoted by I_{3D} and its projection on the 2D plane, denoted by I_{2D} . Most terrain surfaces can be represented as piecewise continuous surfaces. As a result, the corresponding vector field representing the local surface orientation is likely to be rather smooth, excepting regions of surface discontinuity where it may change abruptly. We can express the probability of recovering the vector field of surface normals by means of the Bayes formula:

$$P(\mathcal{V}, \mathcal{E}|I_{3D}, I_{2D}) = \frac{p(I_{3D}|I_{2D}, \mathcal{V}, \mathcal{E})P(\mathcal{V}, \mathcal{E}|I_{2D})}{p(I_{3D}|I_{2D})}, \quad (1)$$

where the probability density $p(I_{3D}|I_{2D}, \mathcal{V}, \mathcal{E})$ models the recovery of the 3D shape, denoted by I_{3D} , from the given 2D projection, its corresponding field of surface normals \mathcal{V} , and the topographic edge map \mathcal{E} . The probability of jointly estimating the vector field of surface normals and the topographic edges using only the given 2D image data is modeled by $P(\mathcal{V}, \mathcal{E}|I_{2D})$, while the probability density $p(I_{3D}|I_{2D})$ models the dependence of the 3D object shape on

the given 2D image. The 3D reconstruction can be made by means of a mesh [46] or as a volumetric image [47]. The conditional probability $P(\mathcal{V}, \mathcal{E}|I_{2D})$ can be further factorized:

$$P(\mathcal{V}, \mathcal{E}|I_{2D}) = p(\mathcal{V}|\mathcal{E}, I_{2D})P(\mathcal{E}|I_{2D}), \quad (2)$$

where the probability $P(\mathcal{E}|I_{2D})$ models the process of recovering topographic edges from the available image data. Finally, the probability density $p(\mathcal{V}|\mathcal{E}, I_{2D})$ models the surface normals resulting from constraints provided by the locations of the topographic edges and the SAR image statistics. The probability associated with edge modeling is described in Section 4, while the probability density corresponding to surface modeling is treated in Section 5. These probabilities will be expressed as energy functions depending on a set of parameters using Gibbs distributions [38]. The maximization of the probabilities corresponds to the minimization of energy functions leading to the estimation of the parameter set.

3 ANALYZING SAR IMAGE CHARACTERISTICS

The probabilities $P(\mathcal{V}, \mathcal{E}|I_{2D})$ and $P(\mathcal{E}|I_{2D})$ from the relationship in (2) depend on the SAR image. In order to estimate these probabilities, in the following section, we derive a statistical model for SAR images.

3.1 The Rayleigh-Bessel Statistical Model

A SAR image is a two-dimensional mapping of received radar signal energy onto a pixel lattice [9]. The radar signal is modulated in quadrature and is represented as a complex number time-series:

$$u(t) = X(t) \cos(\omega t - \beta) + jY(t) \sin(\omega t - \beta), \quad (3)$$

where $X(t)$ is the amplitude of the inphase component, $Y(t)$ is the amplitude of the quadrature component, and ω, β are, respectively, the carrier signal frequency and the phase. The pixel intensity values of the resulting SAR image are given by the amplitude of the complex signal:

$$z(r, a) = \sqrt{X^2(t) + Y^2(t)}, \quad (4)$$

where r and a are, respectively, the SAR image coordinates in the direction perpendicular to the line of flight (range) and parallel to the direction of flight (azimuth). This system of coordinates is nonorthogonal and it is tilted with the antenna depression angle. The pixel values in a SAR image represent contributions from several scatterers. The received signal is distorted by various effects, including intersymbol and cochannel interference, propagation, and electronic device noise [9]. Some of these distortions are compensated in the receiver, while others, besides the physics of interaction between radiation and materials, contribute to the SAR image noise. Let x and y be the independent random variables for the in-phase and quadrature signal components. Furthermore, let us assume that the two random variables are jointly Gaussian, one with the mean μ , the other of zero mean, while their variances, σ^2 , are identical:

$$f(x, y) = \frac{1}{2\pi\sigma^2} \exp\left[-\frac{(x - \mu)^2}{2\sigma^2}\right] \frac{1}{2\pi\sigma^2} \exp\left[-\frac{y^2}{2\sigma^2}\right]. \quad (5)$$

We perform a change of variables into polar coordinates:

$$x = z \sin \theta \quad y = z \cos \theta, \quad (6)$$

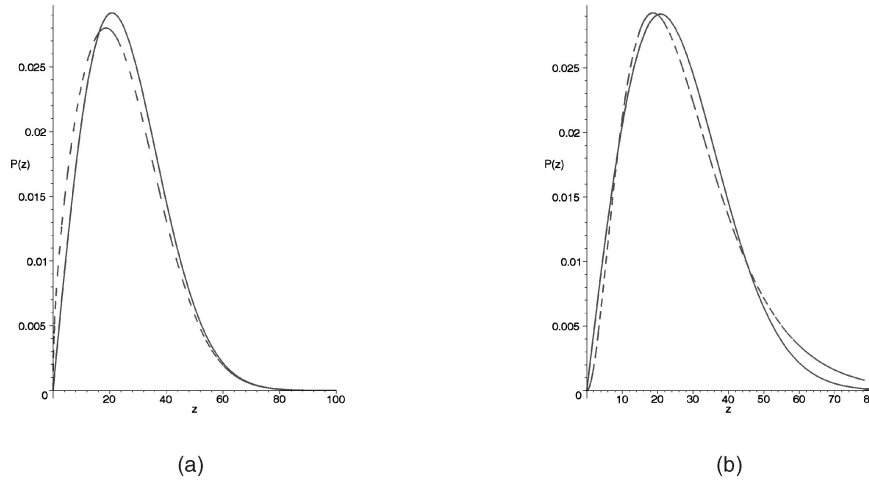


Fig. 1. Rayleigh-Bessel distribution, represented with continuous line, and its approximations, displayed with dashed lines. (a) Rayleigh-Bessel approximation from (9). (b) Comparison with Gamma distribution.

where z and θ are, respectively, the random variables for the amplitude and the polar angle. After transforming the distribution (5) into polar coordinates, as in [48], we obtain the probability density function for the SAR image amplitude variable z from (4) as:

$$\begin{aligned} f_{RB}(z) &= \frac{z}{\pi\sigma^2} \exp\left[-\frac{z^2 + \mu^2}{2\sigma^2}\right] \int_0^\pi \exp\left[\frac{z\mu}{\sigma^2} \cos \theta\right] d\theta \\ &= \frac{z}{\sigma^2} \exp\left[-\frac{z^2 + \mu^2}{2\sigma^2}\right] I_0\left(\frac{z\mu}{\sigma^2}\right), \end{aligned} \quad (7)$$

where $I_0(z\mu/\sigma^2)$ is a zeroth order modified Bessel function of the first kind [49]. This probability density function is a product of two terms. The first one is a Rayleigh distribution which models the additive uncorrelated noise component. The second term is a modified Bessel function of the first kind, which models the signal correlation due to interference. In [33], [36], the SAR image gradient was empirically modeled using a distribution similar to (7).

As in [49], [50], we can use the following first order approximation of the Taylor expansion for simplifying the modified Bessel function, when $|w| \gg 0$:

$$\begin{aligned} I_0(w) &\approx \frac{\exp(w)}{\sqrt{2\pi w}} \left[1 + \frac{1}{8w} + \frac{9}{2!(8w)^2} + \frac{9 \cdot 25}{3!(8w)^3} + \dots \right] \\ &\approx \frac{\exp(w)}{\sqrt{2\pi w}}. \end{aligned} \quad (8)$$

Substituting this approximation into (7), we obtain:

$$f_{RB}(z) \approx \frac{K}{\sigma} \sqrt{\frac{z}{2\pi\mu}} \exp\left[-\frac{(z - \mu)^2}{2\sigma^2}\right], \quad (9)$$

where $K = 1.06$ is a normalization constant. This approximation is valid for $\frac{z\mu}{\sigma^2} \gg 0$. For the purposes of illustration, in Fig. 1a, we show the Rayleigh-Bessel distribution (7) for $\mu = 8$ and $\sigma = 20$ together with its approximation from (9). To measure the similarity between the two distributions $f(z)$ and $g(z)$, we use the Kolmogorov-Smirnov distance:

$$D = \max_{0 < v < \infty} \left| \int_0^v f(z) dz - \int_0^v g(z) dz \right|. \quad (10)$$

The Kolmogorov-Smirnov distance between the Rayleigh-Bessel distribution and its approximation is $D = 0.055$, which indicates that they are statistically very similar.

The Rayleigh distribution, which is a particular case of the distribution appearing in (7) when $\mu = 0$, has been used for modeling radar returns from natural terrain in SAR images [31], [32]. Other studies assume that, after averaging a set of SAR images representing the same scene, the resulting image statistics follow a Gamma distribution [15], [28], [29], [30]. The Gamma distribution is given by:

$$h(z) = \frac{z^{L-1}}{\Gamma(L)m^L} \exp\left(-\frac{z}{m}\right), \quad (11)$$

where L and m are the parameters of the distribution and $\Gamma(L)$ is the Gamma function of order L . We have found that we can obtain a good similarity between the Rayleigh-Bessel and Gamma distributions, appearing in (7) and (11), for a specific set of parameters. The modes of the Rayleigh-Bessel and Gamma distributions coincide when:

$$m = \frac{1}{L-1} \left(\frac{\mu}{2} + \frac{\sqrt{\mu^2 + 2\sigma^2}}{2} \right) \quad (12)$$

and

$$L = m \cdot 0.38. \quad (13)$$

In Fig. 1b, we plot the Rayleigh-Bessel distribution function (7) when its parameters take on the values $\mu = 8$ and $\sigma = 20$. We show the corresponding Gamma distribution with the parameters defined by (12) and (13) in the same figure. The Kolmogorov-Smirnov distance for these two distributions is $D = 0.0414$, which demonstrates the equivalence of the two models when their parameters fulfill (12) and (13).

3.2 Estimating the Parameters of the Rayleigh-Bessel Distribution

In order to use the Rayleigh-Bessel distribution as an image-model for Synthetic Aperture Radar images, we need a means of estimating its parameters. Here, we use the mode of the distribution as a route to parameter estimation. The mode of the distribution represents the most likely value [48] and it can be used as a local brightness estimate. The two

characteristic parameters of the Rayleigh-Bessel distribution (7) are the variance σ^2 , which gauges the spread in the received radar signal, and the parameter μ , which measures the degree of signal interference. The location of the mode corresponds to the position where the first derivative of the probability density function from (9) is zero:

$$\frac{df_{RB}(z)}{dz} = 0 \Rightarrow \hat{\nu} = \frac{\mu}{2} + \frac{\sqrt{\mu^2 + 2\sigma^2}}{2} = \frac{\sigma}{2} \left(\eta + \sqrt{\eta^2 + 2} \right), \quad (14)$$

where we denote the estimate of the mode by $\hat{\nu}$ and the ratio $\eta = \frac{\mu}{\sigma}$.

From Fig. 1, it is clear that the Rayleigh-Bessel is a long tail distribution and, hence, the use of robust statistics is the best route to reliable parameter estimation [39], [40], [51]. To this end, we estimate the mode and the absolute deviation using the median and the median of the absolute deviation from the median (MAD) [39], [41] estimators:

$$\hat{\nu} = \text{Med}\{x_1, x_2, \dots, x_{n \times n}\} \quad (15)$$

$$\hat{\sigma} = \frac{\text{Med}\{|x_1 - \hat{\nu}|, \dots, |x_{n \times n} - \hat{\nu}|\}}{0.6745}, \quad (16)$$

where n represents the window size used for parameter estimation. The interference parameter can be derived from (14):

$$\hat{\mu} = \frac{2\hat{\nu}^2 - \hat{\sigma}^2}{2\hat{\nu}}. \quad (17)$$

The mode of the Rayleigh distribution has the property that $\nu = \sigma$. If we consider the Rayleigh distribution as an extreme case of the Rayleigh-Bessel distribution, we find that (9) and (14) hold when:

$$\eta > 0.5. \quad (18)$$

Next, we assess different estimators for the mode of the Rayleigh-Bessel distribution. The expected value of the mean $E_{Mean}[\hat{\nu}]$ is given by:

$$E_{Mean}[\hat{\nu}] = \int_{-\infty}^{\infty} z f_{RB}(z) dz, \quad (19)$$

where $f_{RB}(z)$ is the Rayleigh-Bessel distribution appearing in (7). The expected value of the median $E_{Med}[\hat{\nu}]$ is located at the position where the probability density function is divided into two equally sized areas [39]. As a result:

$$\int_{-\infty}^{E_{Med}[\hat{\nu}]} f_{RB}(z) dz = \int_{E_{Med}[\hat{\nu}]}^{\infty} f_{RB}(z) dz. \quad (20)$$

Considering the case $\sigma = 20$, for various ratios η in the interval $(0.05, 2)$, we evaluate the expected values provided by the three estimators from (14), (19), and (20). The bias represents the difference between the expected value and the ground-truth parameter. The bias for each estimator is displayed in Fig. 2. As expected, we observe that the median estimator provides a smaller bias than the mean estimator. It is clear from Fig. 2 that, when using (14), we can obtain a small bias for $\eta > 0.5$.

3.3 The Radar Reflectivity Function

Most of the work reported in the literature on shape-from-shading relies on a Lambertian reflectance model. For synthetic aperture radar images, however, Lambert's law

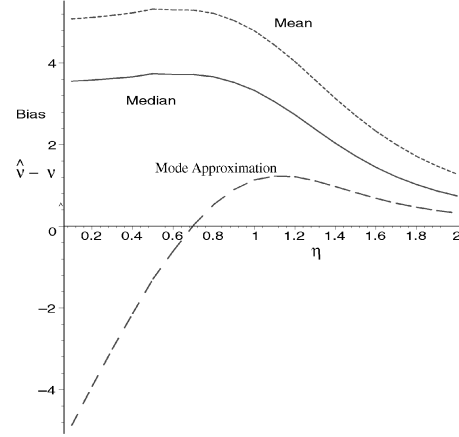


Fig. 2. Bias in estimating the SAR distribution mode when assuming various estimators. The continuous line shows the result of parameter estimation when using median, dotted line when using mean, and dashed line when using (14). The horizontal axis shows the rate $\eta = \mu/\sigma$.

does not provide a good model of the reflectance function. The nature of interaction between the radar beam and the terrain surface is completely different from that between light and matte objects. The variation due to the physics of radiation-material interaction, the type of terrain, the presence of vegetation or man-made objects, the level of humidity, the radar beam wavelength and polarization, and the process of SAR image acquisition each affects the radar reflectivity function [2], [3], [8], [10]. To overcome this problem, in this paper, we preprocess the raw radar data by performing Lambertian correction, circumventing the difficulties described above. In this section, we turn our attention to the estimation of an empirical radar reflectance function, which can be used for the purposes of transforming the radar data into a form to which we can apply a conventional Lambertian shape-from-shading process.

3.3.1 The Lambertian Model

Shape from shading aims to recover local surface orientation from the variation in image intensity [12], [19], [20], [27]. Usually, the surface under study is assumed to be matte and to exhibit Lambertian reflectance [18], [19]. Under this restriction, the observed intensity is proportional to the cosine of the incidence angle, i.e., the scalar product between the unit vectors in the directions of the illuminant and the surface normal:

$$I(r, a) = \cos \gamma = \mathbf{N}^T \mathbf{L}, \quad (21)$$

where the image intensity $I(r, a)$ is normalized to fall within the interval $[0, 1]$. The unit vector in the surface normal direction at the location (r, a, h) is given by

$$\mathbf{N} = \frac{1}{\sqrt{1 + p^2 + q^2}} (-p, -q, 1)^T, \quad (22)$$

where $p = \frac{\partial h}{\partial a}$ and $q = \frac{\partial h}{\partial r}$ are the components of the surface gradient in the r (range) and a (azimuth) directions. The unit vector in the surface normal direction is given by

$$\mathbf{L} = (\cos \tau \sin \alpha, \sin \tau \sin \alpha, \cos \alpha)^T, \quad (23)$$

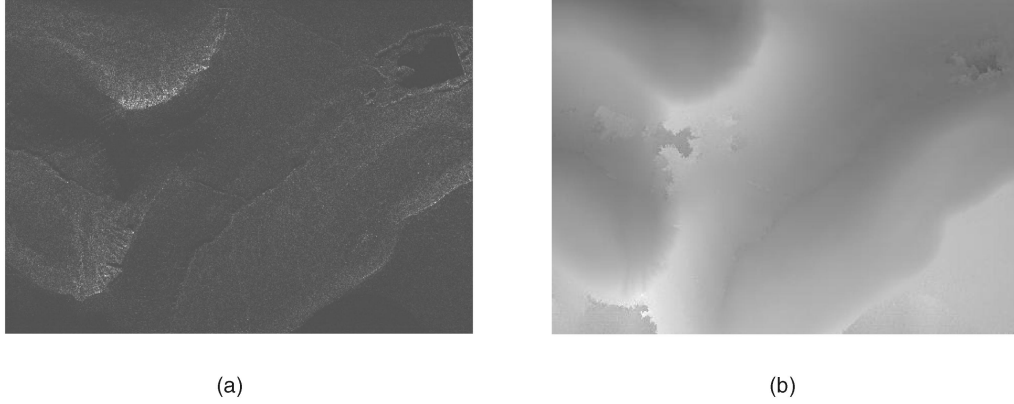


Fig. 3. Synthetic Aperture Radar (SAR) image and its corresponding Digital Elevation Map (DEM). (a) Original SAR image mapped in a shifted range of graylevel values for better visibility. (b) Digital elevation map.

where τ is the azimuthal angle and α is the inclination angle with the plane defined by the optic axis and the azimuthal direction, i.e., the (h, a) plane. With these ingredients,

$$\cos \gamma = \frac{\cos \alpha - p \cos \tau \sin \alpha - q \sin \tau \sin \alpha}{\sqrt{1 + p^2 + q^2}}. \quad (24)$$

3.3.2 SAR Reflectivity Function

As noted above, due to their physics of formation, SAR images do not exhibit Lambertian reflectance properties [11], [27]. One of our aims in this paper is to apply a correction process to the measured radar reflectance function so that conventional Lambertian shape-from-shading methods can be applied to SAR images. In this section, we consider how to perform this reflectivity transformation.

Provided that the radar illumination is directed along the range direction ($\tau = 0$), then the reflectivity equation for SAR images is:

$$\cos \gamma = \mathcal{R} \left(\frac{\cos \alpha - p \sin \alpha}{\sqrt{1 + p^2 + q^2}} \right), \quad (25)$$

where \mathcal{R} is the reflectivity function, which is unknown for the nonLambertian case. We can make an empirical estimate of \mathcal{R} provided that we have at hand a digital elevation map (DEM) with ground truth height information for a given SAR image. Let us suppose that the DEM and SAR images are aligned so that pixel correspondences are known. For the SAR image, we can estimate $\cos \gamma$ from the normalized intensity $I(r, a)$. On the other hand, the DEM image provides us with estimates of the components p and q of the surface height gradient. By choosing a suitable empirical parametric function, we can model the correspondence between the two data sets.

3.3.3 Empirical Derivation of the Reflectivity Function

To illustrate the method outlined in the previous section, we turn our attention to the SAR image shown in Fig. 3a, which was collected over a mountainous region in Wales. The size of this image is $1,850 \times 1,320$ pixels and corresponds to C-band (5.7 GHz) radar with a bandwidth of 90MHz and a peak power of 9.4 W, taken at an antenna depression angle $\gamma = 20$ degrees. The resolution of the image is at 1.905m in azimuth and 1.499m in range. The main point to note is that the terrain features are not clear in this image due to the nonlinear characteristics of the reflectance function. Its corresponding DEM is shown in Fig. 3b and has a size of 462×330 . The

sampling in this image is, therefore, 7.62m in azimuth by 5.996m in range. The depth provided in this DEM was obtained by phase unwrapping in interferometric SAR imaging, given two SAR images taken with a stereo antenna system [52]. Several artifacts due to the radar image acquisition process can be observed in this DEM image. For the purposes of modeling the reflectivity function, we calculate the gradient for each pixel of the DEM image and its corresponding normal orientation angle using (25), and we equate it to the median estimate from the corresponding block of pixels of the SAR image. The inverse of the reflectivity function is represented with a dashed curve in Figs. 4a and 4b. The shape of this reflectivity function is characteristic of SAR images [2], [3]. We have tested two empirical models for the inverse of the reflectivity function. The first is a single continuous function over the entire domain:

$$\mathcal{R}^{-1}(I(r, a)) = \frac{I(r, a) - 55}{0.8 \cdot I(r, a)}. \quad (26)$$

This model is shown in Fig. 4a, with a continuous line. The second model, shown in Fig. 4b, consists of a piecewise polynomial approximation, where the first branch is modeled by a polynomial of fourth order and the second branch by a polynomial of second order. The transformations of the original SAR image from Fig. 3a obtained using the inverse reflectance functions plotted in Figs. 4a and 4b, are shown in Figs. 4c and 4d, respectively. Despite the fact that the piecewise polynomial approximation is more accurate in modeling the inverse of the reflectance curve, there is no great difference in the quality of the transformed SAR images from Figs. 4c and 4d. Due to its simplicity and continuity over the entire domain of interest, we choose to use the reflectivity function, whose inverse is provided in (26), as the empirical reflectance model.

4 FINDING SALIENT TERRAIN FEATURES IN SAR IMAGES

In Section 2, shape-from-shading was posed as maximum a posteriori (MAP) estimation. In order to maximize the probability $P(\mathcal{V}, \mathcal{E} | I_{2D})$, we need to maximize each of its components from (2). In this section, we model the edge-map probability $P(\mathcal{E} | I_{2D})$, appearing on the righthand side of (2). In SAR images of terrain, edges can be associated with terrain features such as ridges and ravines, but also with changes in radar image albedo or other changes in

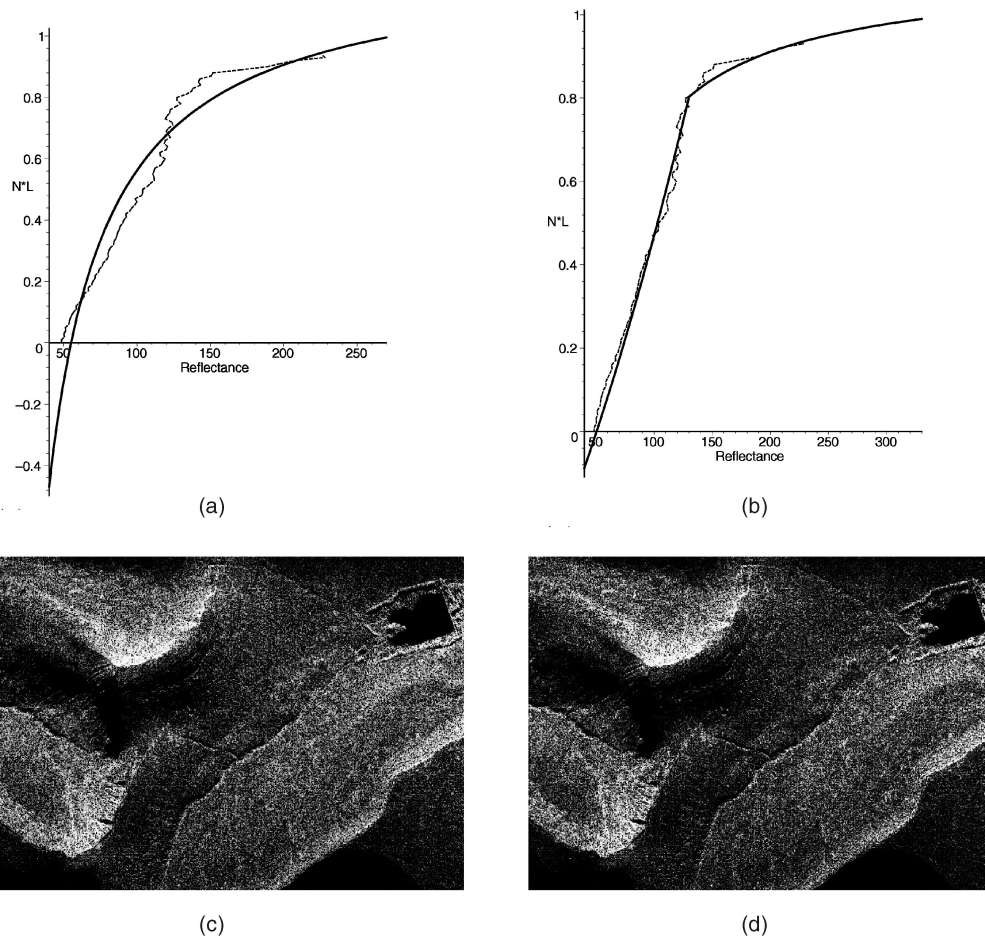


Fig. 4. Modeling SAR image reflectance function. (a) Approximation of the reflectance function using (26). (b) The reflectance function approximated by a piecewise polynomial function. (c) SAR image recovery after modeling the reflectance function using (26). (d) SAR image recovery after modeling the reflectance function using piecewise polynomial approximation.

local statistics. The existence of isolated terrain features which are limited in size is unlikely. In order to avoid edge discontinuities, we use a Markov Random Field (MRF) model [53] which enforces connectivity among the detected edge segments. The edge-map probability is computed using the approach adopted by Hancock and Kittler [54]:

$$P(\mathcal{E}|I_{2D}) = \prod_j \left[\frac{P(\mathcal{E}_j|I_{2D})}{P(\mathcal{E}_j)} P(\mathcal{E}_j|\mathcal{E}_i \in \mathcal{N}_j) \right], \quad (27)$$

where j denotes a component edge, $P(\mathcal{E}_j|I_{2D})$ is the a posteriori probability of the j th edge segment, $P(\mathcal{E}_j|\mathcal{E}_i \in \mathcal{N}_j)$ is the probability of connecting an edge segment \mathcal{E}_j with another edge segment \mathcal{E}_i from its neighborhood, and $P(\mathcal{E}_j)$ is the a priori probability of an edge segment. According to this approach, the edge map probability consists of two terms. The first term is a product over edge segment detection probabilities. The second term is the prior for the neighborhood edge configuration.

The maximization of the edge probability $P(\mathcal{E}_j|I_{2D})$ can be accomplished using a maximum likelihood edge detector. The maximum likelihood process requires the estimation of the underlying image distribution. Several algorithms have been proposed for edge detection in SAR images. In [28], [55], a Ratio-of-Averages edge detector was used for speckle images. This edge detector was shown to be optimal when the SAR image follows a Gamma distribution [29]. In this paper,

we model SAR terrain images using a Rayleigh-Bessel distribution (7). Furthermore, as shown in Section 3.1, this distribution can be replaced by the approximation in (9). We pose edge detection as a hypothesis testing problem [29], [56]. As described in [29], the maximum log-likelihood ratio λ_j between two neighboring regions from a SAR image, denoted by j and $j+1$, is:

$$\lambda_j = |\ln[p(z|I_{2D,j})] - \ln[p(z|I_{2D,j+1})]|, \quad (28)$$

where $p(z|I_{2D,j})$ is the approximation in the Rayleigh-Bessel distribution appearing in (9) and corresponding to the region j from the image I_{2D} . The parameters of the Rayleigh-Bessel distribution are estimated using the method outlined in Section 3.2. The probability $P(\mathcal{E}_j|I_{2D})$ from (27) is maximized when the likelihood ratio λ_j is maximized. This situation corresponds to a discontinuity in the image statistics. If the probabilities of the two regions are equal, then no salient features are present and $\lambda_j = 0$. Let us consider the region j to be characterized by the parameters (μ_1, σ_1) and to contain k pixels. Similarly, the region $j+1$ has the parameters (μ_2, σ_2) and contains $n^2 - k$ pixels. Here, n is the size of the window used for edge detection, which contains the regions j and $j+1$. The probability distribution for the observed SAR amplitude in the j th region is given by:

$$p(z|I_{2D,j}) = \prod_{i=1}^k \frac{1}{\sigma_1} \sqrt{\frac{I_i}{2\pi\mu_1}} \exp\left[-\frac{(I_i - \mu_1)^2}{2\sigma_1^2}\right], \quad (29)$$

where I_i is the SAR amplitude for the pixel i . Let us consider that the number of pixels in the two regions is equal, i.e., $k = n^2/2$. After taking logarithms, the log-likelihood ratio from (28) becomes:

$$\lambda_j = \left| \ln\left(\frac{1}{\hat{\sigma}_1} \sqrt{\frac{\hat{I}_j}{2\pi\hat{\mu}_1}}\right) - \frac{(\hat{I}_j - \hat{\mu}_1)^2}{2\hat{\sigma}_1^2} - \ln\left(\frac{1}{\hat{\sigma}_2} \sqrt{\frac{\hat{I}_{j+1}}{2\pi\hat{\mu}_2}}\right) + \frac{(\hat{I}_{j+1} - \hat{\mu}_2)^2}{2\hat{\sigma}_2^2} \right|, \quad (30)$$

where \hat{I}_j and \hat{I}_{j+1} are the estimates of the SAR amplitude in the regions j th and $(j+1)$ th. The maximum likelihood of the Rayleigh-Bessel function occurs at the mode of the distribution, as shown in Section 3.1. If we replace $\hat{\mu}$ with its maximum-likelihood estimate from (17), we obtain the following log-likelihood ratio:

$$\lambda_j = \left| \ln\left(\frac{1}{\hat{\sigma}_1 \sqrt{1 - \frac{\hat{\sigma}_1^2}{2\hat{\nu}_1^2}}}\right) - \ln\left(\frac{1}{\hat{\sigma}_2 \sqrt{1 - \frac{\hat{\sigma}_2^2}{2\hat{\nu}_2^2}}}\right) - \frac{\hat{\sigma}_1^2}{8\hat{\nu}_1^2} + \frac{\hat{\sigma}_2^2}{8\hat{\nu}_2^2} \right|, \quad (31)$$

where $\hat{\nu}_j$ is the estimated mode from (15) and $\hat{\sigma}_j$ is the estimate of the absolute deviation from (16), both for the j th region.

In order to obtain reliable statistical estimates, we must use a large window size n [55]. However, by using a large window size, we recover thick edges. To overcome this problem, we perform edge thinning by using an erosion operator [57]. Edge thinning is done in such a way that it preserves the connectivity among different edge elements while maximizing the edge neighborhood probability $P(\mathcal{E}_j|\mathcal{E}_i \in \mathcal{N}_j)$. The connectivity among separate edge segments is enforced using a two-threshold hysteresis linking scheme [54]. If the log-likelihood for a SAR region exceeds a threshold value, then that region is labeled as an edge. When the log-likelihood falls between the two thresholds, then that region is labeled as an edge only if it connects two other previously labeled edge segments. Small edge segments which do not exhibit this connectivity property are eliminated.

Ridges are the peaks of structures of convex terrain topography and are characterized by a sharp decrease in the brightness when traversed in the illuminant direction. Ravines, on the other hand, correspond to bottoms of concave terrain features and are characterized by a sharp increase in the brightness when the boundary between a back-slope and a slope is traversed in the illuminant direction. These properties are used to classify the maximum log-likelihood edges as either ridges or ravines. The median estimator has been shown to be more robust than the mean when decision making is attempted using overlapping class probability densities [41]. In our case, edge classification is performed using a decision test which compares the median estimate of the radar return from two rectangular regions, oriented in the range direction, on either side of the given edge:

$$t_E = \frac{\text{Med}\{I(r, a)|r_E - d < r < r_E\}}{\text{Med}\{I(r, a)|r_E < r < r_E + d\}}, \quad (32)$$

where r_E is the range coordinate of the edge and d is the width of the region used for the topographic test, in the range direction. When the edge test statistics, t_E , is above a

threshold, then we classify it as a ridge. When this condition is not met, then the edge is classified as a ravine. This type of detector will also respond to rivers, which can easily be assimilated with ravines, man-made objects, and can be influenced by changes in albedo.

5 SHAPE-FROM-SHADING IN SAR IMAGES

The shape from shading problem has been cast in a maximum a posteriori framework in Section 2. In this section, we show how we can estimate the probability density $p(\mathcal{V}|\mathcal{E}, I_{2D})$, which represents the recovery of the vector field of surface normals from the SAR image using the available terrain features. We can represent the vector field of surface normals by means of a Markov Random Field [53]. This model decomposes the needle-map probability $p(\mathcal{V}|\mathcal{E}, I_{2D})$ using the a posteriori probability of the local surface normal $p(\mathcal{V}_j|\mathcal{E}_j, I_{2D})$ and the conditional needle-map probabilities $P(\mathcal{V}_j|\mathcal{V}_i \in \mathcal{N}_j)$ of the surface normals \mathcal{V}_j depending on their neighborhood $\mathcal{V}_i \in \mathcal{N}_j$:

$$p(\mathcal{V}|\mathcal{E}, I_{2D}) = \prod_j p(\mathcal{V}_j|\mathcal{E}_j, I_{2D})P(\mathcal{V}_j|\mathcal{V}_i \in \mathcal{N}_j). \quad (33)$$

Several SFS approaches have been proposed for Lambertian objects. Horn and Brooks [19] have developed a variational framework for SFS. According to their approach, there is a soft data-closeness term, which models compliance with the image irradiance equation, and a smoothing term, which regularizes (i.e., smoothes) the recovered needle map. However, this algorithm has the tendency to oversmooth the recovered vector field. Worthington and Hancock [20] rendered the process robust by using the image irradiance equation as a hard constraint rather than a data closeness constraint. In this approach, the surface normals must always lie on the surface of a cone, with the axis pointing in the illuminant direction. The apex angle of the cone is given by:

$$\gamma = \arccos(\mathbf{N}^T \mathbf{L}), \quad (34)$$

where \mathbf{N} is the surface normal and \mathbf{L} is the illuminant orientation. In our maximum a posteriori framework, the data-closeness and smoothness terms are captured by the a posteriori probability of the local surface normals $p(\mathcal{V}_j|\mathcal{E}_j, I_{2D})$ and by the smoothness prior $P(\mathcal{V}_j|\mathcal{V}_i \in \mathcal{N}_j)$ from (33). These probabilities are modeled by means of energy functions [38]. Thus, the probability maximization task is transformed into an energy minimization problem.

5.1 Vector Field Initialization

As noted above, the amplitude of a SAR image does not follow the Lambertian reflectance model. In order to apply shape-from-shading to SAR images, we must first perform Lambertian correction by applying the inverse of the reflectance function \mathcal{R}^{-1} , given in (26), to the raw radar data. In the case of SAR images, the signal variance, σ^2 , causes an uncertainty in the estimation of the brightness. In this situation, the irradiance cone defined in [20] must be replaced by a conical envelope which spans a range of apex angles, determined by the transformed radar reflectance and the radar signal variance. The range of cosines of the cone apex angle is defined to fall in the following interval:

$$\cos(\gamma(t)) \in \left[\cos(\hat{\gamma}(0)) - \frac{\hat{\sigma}}{4}, \cos(\hat{\gamma}(0)) + \frac{\hat{\sigma}}{4} \right], \quad (35)$$

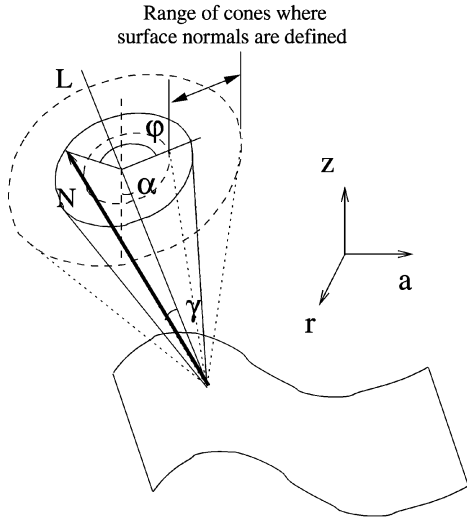


Fig. 5. The range of cones defining local surface normals when illuminating a 3D surface in SAR images.

where $\hat{\gamma}(0)$ corresponds to the orientation of the initial surface normal calculated for the mode of the local SAR distribution and $\hat{\sigma}$ is the absolute deviation estimated using (16). The conical envelope is illustrated in Fig. 5.

The parameter μ , estimated using (17), corresponds to the level of interference from various scattering elements. This parameter can be used for distinguishing different types of terrain. Water strongly absorbs electromagnetic energy and is characterized by the lowest range of values for the interference parameter μ . Since the surface of water is horizontal, the associated surface normals are parallel to the z axis. Shadow regions correspond to back slopes and they are also characterized by low values of μ . The surface normals for such regions may subtend rather large angles with the illumination direction. Layover regions have a larger brightness and are characterized by higher values for μ .

In shape-from-shading, there is a bas-relief ambiguity caused by the fact that both concave and convex surfaces produce the same variation in brightness [20]. This ambiguity can be resolved using boundary constraints. As pointed out in Section 4, we use the direction of variation in brightness at edges in order to classify them as either ridges or ravines. Naturally, the ridges belong to concave surfaces, while ravines belong to convex surfaces. As a result, ravines are attractors for the surface normals. On the other hand, ridges can be seen as repelling surface normals. In order to capture these features, we model the a posteriori needle-map probability as an energy function:

$$p(\mathcal{V}_j | \mathcal{E}_j, I_{2D}) \simeq \frac{1}{Z} \exp\{-|\mathcal{R}^{-1}(I_j(r, a)) - \mathbf{N}_j^T \mathbf{L}| - |\mathbf{N}_j^T \mathbf{E}_l|\}, \quad (36)$$

where Z is a normalizing constant, \mathbf{E}_l is the tangent vector to the closest edge from the surface normal \mathbf{N}_j . The first term in the exponential models the recovery of the needle-map from the corrected reflectivity information. The second term models the effect of constraints provided by the whereabouts of terrain features and the direction of the local surface normals. This term is modeled using the scalar product between the surface normal and the tangent vector of the nearest edge. According to the test function t_E appearing in (32), the surface normal is directed toward a ravine and away from a ridge, as shown in Fig. 6. Ridges are associated with divergent flow patterns in the vector field of surface normals.

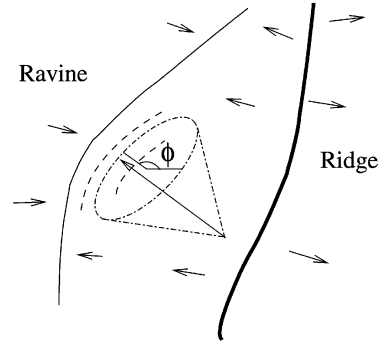


Fig. 6. Surface normal orientation in the horizontal plane depends on the nearest edge classification. Thick lines represent ridges while thin lines mark ravines. Dashed lines show the range of values for the surface normal vector.

Ravines, on the other hand, are associated with convergent flow patterns. By means of this energy function, the maximization of the probability density $p(\mathcal{V}_j | \mathcal{E}_j, I_{2D})$ leads to a suboptimal estimate of both the cone apex angle γ and the azimuthal angle ϕ (the angle between the surface normal projection in the (r, a) plane and the azimuth direction). When $t_E > 1$:

$$\cos \phi = \frac{l_a - j_a}{\|\mathbf{l} - \mathbf{j}\|}, \quad (37)$$

where $\mathbf{j} = (j_r, j_a)$ and $\mathbf{l} = (l_r, l_a)$ are the locations of the surface normal vector and its closest edge, respectively. We can derive a similar relation for $\sin \phi$. For $t_E < 1$, the signs of $\cos \phi$ (37) and $\sin \phi$ are negated (corresponding to the angle $\phi + \pi$).

We have shown how to estimate the opening angle of the radar reflectance cone, γ , and the orientation angle of the surface normal projection onto the image plane, denoted by ϕ . In the case of SAR images, the azimuthal angle of the radar beam is $\pi/2$, while the inclination angle with the (h, a) plane is denoted by α , as in Section 3.3. The radar reflectance cone is rotated by the angle α with respect to the image plane. In rectangular coordinates, the surface normal is given by:

$$\mathbf{N}^T = [\sin \gamma \sin \phi \quad \sin \gamma \cos \phi \quad \cos \gamma] \cdot \begin{bmatrix} \cos \alpha & 0 & -\sin \alpha \\ 0 & 1 & 0 \\ \sin \alpha & 0 & \cos \alpha \end{bmatrix}. \quad (38)$$

The components of \mathbf{N} are:

$$\begin{aligned} \mathbf{N} &= [N_r \quad N_a \quad N_h] \\ &= [\sin \gamma \sin \phi \quad \cos \alpha + \cos \gamma \sin \alpha \quad \sin \gamma \cos \phi \\ &\quad - \sin \gamma \sin \phi \quad \sin \alpha + \cos \gamma \cos \alpha]. \end{aligned} \quad (39)$$

This is the initial direction of the surface normal that maximizes the probability density function $p(\mathcal{V}_j | \mathcal{E}_j, I_{2D})$ from (36).

5.2 Vector Field Smoothing

Since shape-from-shading is an “ill-posed” problem, the probability in (36) can be simultaneously maximized by several different surface normals. Additional constraints are necessary in order to obtain a solution and resolve ambiguities. Here, we model the smoothness prior $P(\mathcal{V}_j | \mathcal{V}_i \in \mathcal{N}_j)$ from (33) using a local clustering energy:

$$P(\mathcal{V}_j | \mathcal{V}_i \in \mathcal{N}_j) \simeq \frac{1}{Z} \exp \left\{ - \sum_{i \in \mathcal{N}_j} \psi(\mathbf{N}_i, \mathcal{N}_j) \right\}, \quad (40)$$

where $\psi(\mathbf{N}_i, \mathcal{N}_j)$ is a regularization function depending on the surface normals from a neighborhood \mathcal{N}_j of the j th site and Z is a normalizing constant. This probability is maximized when the surface normals from the same neighborhood have similar directions.

Commencing from the initial surface normal direction as derived in the previous section, we smooth the needle-map with the goal of maximizing the smoothness prior $P(\mathcal{V}_j | \mathcal{V}_i \in \mathcal{N}_j)$. The Euclidean distance can be employed for calculating the similarity of neighboring surface vectors [19]:

$$\psi(\mathbf{N}_i, \mathcal{N}_j) = \|\mathbf{N}_i - \mathbf{N}_j\|, \quad (41)$$

where $\|\cdot\|$ denotes the Euclidean distance between two neighboring vectors at sites i and j . Minimization of this regularization function can be performed using adaptive local averaging, as in [19]. At iteration $t + 1$, the updated surface normals are given by:

$$\hat{\mathbf{N}}_j(t+1) = \hat{\mathbf{N}}_j(t) - \varepsilon \left[\hat{\mathbf{N}}_j(t) - \frac{\sum_{i \in \mathcal{N}_j} \hat{\mathbf{N}}_i(t)}{R} \right], \quad (42)$$

where $\varepsilon \in (0, 1)$ is the updating rate and R is the number of sites from the neighborhood \mathcal{N}_j of the site j .

Robust statistics [39], [51] have proven to be very useful in image processing and computer vision [40] when the raw data is corrupted by impulse noise or displays a long tailed distribution due to outliers. Recently, Worthington and Hancock [20] have shown how robust functions can be used as regularizers $\psi(\mathbf{N}_i, \mathcal{N}_j)$ in order to smooth surface normal needle maps in the presence of surface discontinuities. In this section, we take these ideas one step further by considering various robust estimators for smoothing surface normals.

The first alternative is to use the marginal median to smooth the needle-map [41]. The updated surface normal direction is given by:

$$\hat{\mathbf{N}}_j(t+1) = \text{Med}_{l \in \mathcal{N}_j} \{ \hat{\mathbf{N}}_l \}, \quad (43)$$

where the median estimator is applied on each component of the surface normal vector separately.

The second robust estimator considered in this study is the vector median [42]. This estimator selects the vector which has the lowest sum of Euclidean distances to the remaining vectors from the given neighborhood \mathcal{N}_j :

$$\hat{\mathbf{N}}_j(t+1) = \hat{\mathbf{N}}_l(t), l = \arg \min_k \sum_{i \in \mathcal{N}_j} \|\hat{\mathbf{N}}_k - \hat{\mathbf{N}}_i\|, \quad (44)$$

where $k \in \mathcal{N}_j$.

Worthington and Hancock proposed several robust methods for smoothing surface normal fields [20]. Each of these algorithms has been shown to outperform the Horn and Brooks approach [19]. The best results are obtained when using a curvature consistency algorithm. The smoothing achieved after applying this algorithm is stronger in regions of uniform local topography. At the boundary between regions with different topographic or curvature class, the smoothing is less strong. The robust regularizer used for needle map smoothing in [20] is:

$$\psi(\mathbf{N}_i, \mathcal{N}_j) = \rho_s \left(\left\| \frac{\partial \mathbf{N}_j}{\partial x} \right\| \right) + \rho_s \left(\left\| \frac{\partial \mathbf{N}_j}{\partial y} \right\| \right), \quad (45)$$

where ρ_s is a robust kernel of width parameter s , $i \in \mathcal{N}_j$, and the derivatives are calculated in the neighborhood \mathcal{N}_j . The most effective robust error kernel was found to be the Huber function [51]:

$$\rho_s(z) = \frac{s(N_j)}{\pi} \log \cosh \left(\frac{\pi z}{s(N_j)} \right). \quad (46)$$

In [20], Worthington and Hancock impose curvature consistency by adapting the kernel width $s(N_j)$ using a variation of the Koenderick and van Doorn shape index [58]. The kernel width is set equal to:

$$s(N_j) = s_0 \exp \left[- \left(\frac{1}{R} \sqrt{\sum_{i \in \mathcal{N}_j} \frac{(q(i) - q(j))^2}{\Delta q^2}} \right) \right], \quad (47)$$

where $q(i)$ is the shape index for a site i from the neighborhood of the site j and $\Delta q = 1/8$ is the average difference in shape index between the center values of adjacent curvature classes. The shape index is calculated from the Hessian of the surface and can be expressed as a function of local surface normals:

$$q(j) = \frac{2}{\pi} \arctan \frac{\frac{\partial N_a}{\partial a} + \frac{\partial N_r}{\partial r}}{\sqrt{\left(\frac{\partial N_a}{\partial a} - \frac{\partial N_r}{\partial r} \right)^2 + 4 \frac{\partial N_a}{\partial r} \frac{\partial N_r}{\partial a}}}, \quad (48)$$

where the components of the normal vector are denoted as $\mathbf{N}_j = [N_a, N_r, N_h]^T$. The surface normals are updated by performing gradient descent on the robust regularizer:

$$\hat{\mathbf{N}}_j(t+1) = \hat{\mathbf{N}}_j(t) - \varepsilon \frac{\partial \psi(\mathbf{N}_i, \mathcal{N}_j)}{\partial \mathbf{N}_j}. \quad (49)$$

The differentiation of the regularizer function (45) is provided in [20].

After updating the surface normal directions, we back-project them onto the radar reflectance cone. The sine of the updated angles γ and ϕ are:

$$\begin{aligned} \sin \gamma &= \sqrt{\hat{N}_a^2 + (\hat{N}_r \cos \alpha - \hat{N}_h \sin \alpha)^2} \\ \sin \phi &= \frac{\hat{N}_r \cos \alpha - \hat{N}_h \sin \alpha}{\sin \gamma}. \end{aligned} \quad (50)$$

The surface normal is constrained to fall within the envelope described by a family of irradiance cones. The mode of the local SAR distribution provides the central illuminance cone, while the variance defines the extent of the envelope. The apex angle range for the envelope is given by (35). After updating the surface normal according to (50), we require that it takes a value $\hat{\gamma}(t)$ which falls within the envelope defined by (35). If the value of $\hat{\gamma}(t)$ falls outside the interval of acceptable values, then we force it to the closest boundary of the interval, and update the surface normal direction accordingly. The envelope within which the surface normal is free to move is illustrated with dashed lines in Figs. 5 and 6. The shape-from-shading algorithm initialized using the surface normal directions provided in (38) is iterated to maximize the probability appearing in (40), while maintaining the data closeness constraint of (36). Convergence is reached when the vector field of surface normals does not change significantly between two consecutive iterations.

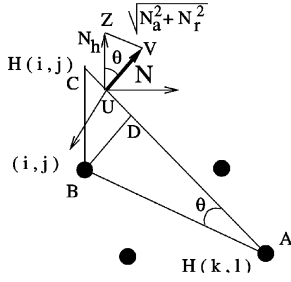


Fig. 7. The evaluation of 3D height information.

5.3 3D Height Reconstruction

In the preceding sections of this paper, we have described how to recover the field of surface normals from radar data that has been subjected to Lambertian reflectivity correction. However, in most terrain analysis problems, the goal is the reconstruction of the surface height function. When having two images taken by two antennas, we can use phase unwrapping for 3D surface reconstruction [52]. However, in the case analyzed in this paper, we are provided with only one image. In the previous sections, we have shown how we can estimate a field of surface normals from a single SAR image. Formally, we are interested in the problem of reconstructing a surface from a Gauss map. In this section, we describe a simple surface integration method that can be used to reconstruct surface height from local surface orientation information [43]. The suggested height estimation algorithm is iterative. At each iteration, the calculation of height is a two step process. In the first step we decide which neighboring site is appropriate to be used as reference for estimating the unknown height, while, in the second stage, we estimate its height.

We wish to estimate the surface height at the point B which has site coordinates (i, j) . This site is a neighbor of the location A which has site coordinates (r, a) and known height. Hence, $(i, j) \in \mathcal{N}(r, a)$. Let the perpendicular to the image plane at location B intersect the surface at location C , and let the known height of this location be $H(i, j)$. Further, let $\|BC\|$ represent the difference in surface height for locations A and B on the image plane. Since the height at B is unknown, we must select from its set of neighbors the reference site of predetermined height from which we can make the most reliable height estimate. The selection of the reference site proceeds as follows: First, we construct the plane formed by the surface normal vector at the site B and the perpendicular at that site, i.e., BC . Next, we compute the distances from all the sites $(i, j) \in \mathcal{N}(r, a)$ to this plane, as

$$d(a, r) = \frac{|(a - j)N_a - (r - i)N_r|}{\sqrt{N_a^2 + N_r^2}}. \quad (51)$$

We search for sites which minimize this distance. To do this, we set a distance threshold f . This distance threshold is initially taken as $f = 0$, i.e., we test if A is located on the plane formed by BC and the surface normal. At every iteration, for each site from the entire lattice, we choose only those locations which fulfill the condition:

$$d(a, r) \leq f. \quad (52)$$

By finding the minimum of $d(a, r)$ for all the sites of known height that fulfill (52) in the neighborhood $\mathcal{N}(i, j)$, we select the site (k, l) at which to update the height. The site is the one that satisfies the condition:

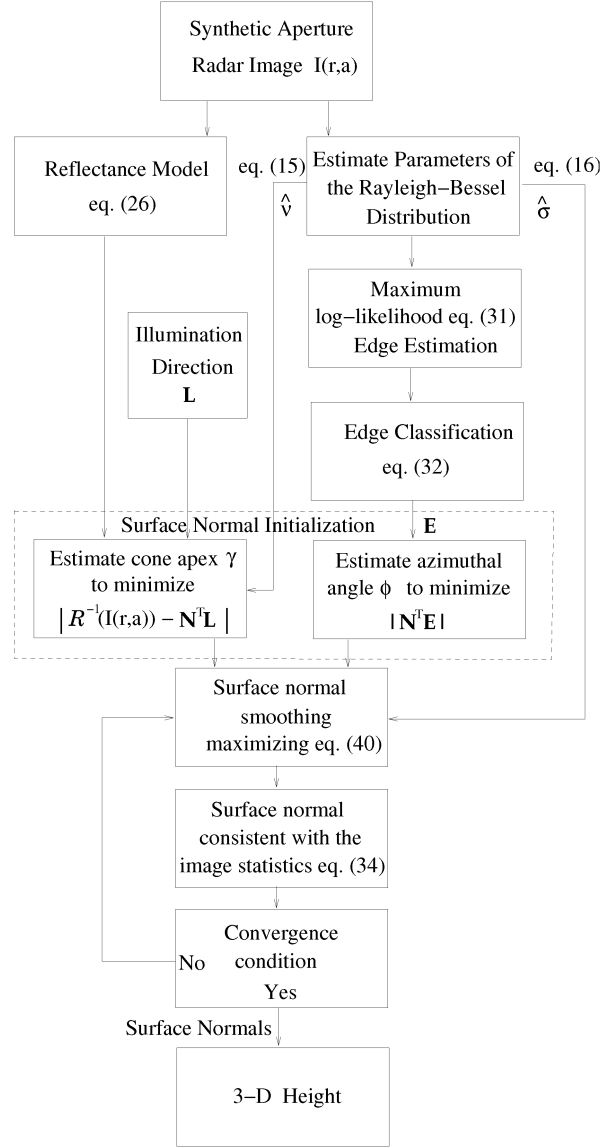


Fig. 8. Processing stages of the radar shape-from-shading algorithm.

$$(k, l) = \arg \min_{(a, r) \in \mathcal{N}(i, j)} \{d(a, r)\}. \quad (53)$$

In the case when $N_a = 0$, we compute the modified distance

$$d(a, r) = \max\{|a - j|, |r - i|\}, \quad (54)$$

where $(i, j) \in \mathcal{N}(a, r)$.

In the second stage, the height $H(i, j)$ is computed using simple trigonometry. The reference site A of known height and the site B of unknown height are shown in Fig. 7. From this figure, it is clear that we can use the similarity of two triangles to estimate the unknown height. The first triangle is formed by the surface normal vector and the h axis (which is parallel with BC) and it is denoted by UVZ . The second triangle, denoted by ABC , is formed by the sites A and B on the image plane and the location C on the surface, i.e., the point at which we estimate the height. From the similarity of these triangles, we have:

$$\frac{\|BC\|}{\|ZV\|} = \frac{\|AB\|}{\|UZ\|} = \frac{\|AC\|}{\|UV\|}, \quad (55)$$

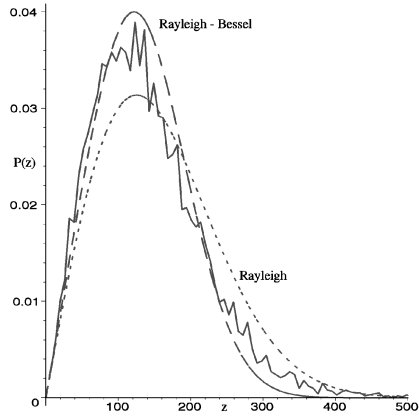


Fig. 9. Fitting the SAR image distribution with Rayleigh and Rayleigh-Bessel models.

where $\|AB\|$ represents the distance between the neighboring sites A and B , $\|BC\|$ denotes the difference of height:

$$\|BC\| = |H(i, j) - H(k, l)|. \quad (56)$$

After replacing the distances in (55), we get:

$$\frac{|H(i, j) - H(k, l)|}{\sqrt{N_r^2 + N_a^2}} = \frac{\sqrt{(l-j)^2 + (k-i)^2}}{N_h} = \frac{\|AC\|}{1}, \quad (57)$$

where $H(i, j)$ is the height for the site (i, j) and $H(k, l)$ is the known height at the reference location (k, l) , chosen according to the condition in (53). From this relationship, it is clear that, when $N_h \rightarrow 0$, then $H(i, j) \rightarrow \infty$. This can lead to discontinuities in the height estimation process.

In order to avoid discontinuities, we must ensure that the reconstructed surface is finite. Let us consider the projection of the location B onto the surface and let this point be denoted by D . We assume that the height $\|BC\|$ at site (i, j) is approximated by $\|BD\|$. This simplification will ensure that we avoid singularities in the case when reconstructing the surface height from the field of surface normals. In this case, using the similarity between the triangles ABD and UVZ , we find that:

$$\frac{\|BD\|}{\|ZV\|} = \frac{\|AB\|}{\|UV\|} = \frac{\|AD\|}{\|UZ\|}. \quad (58)$$

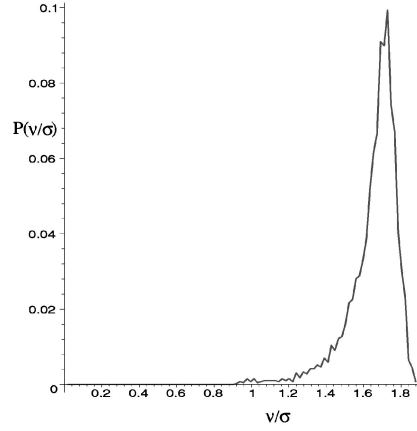


Fig. 10. Distribution of the ratio between the mode and absolute deviation.

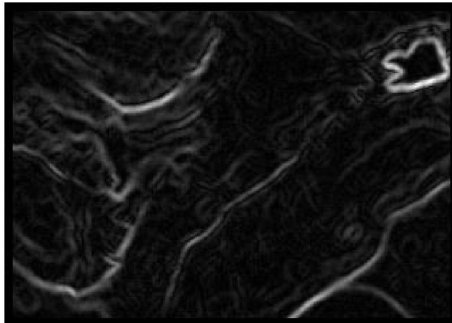
Substituting for the distances in the above equation, we obtain

$$\frac{|H(i, j) - H(k, l)|}{\sqrt{N_r^2 + N_a^2}} = \frac{\sqrt{(l-j)^2 + (k-i)^2}}{1} = \frac{\|AD\|}{N_h}. \quad (59)$$

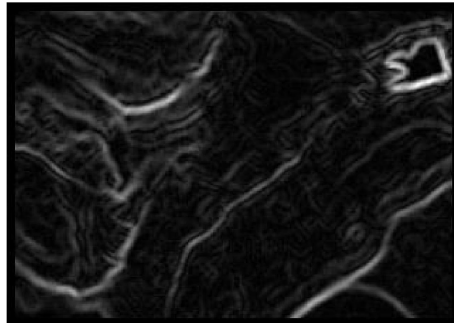
As a result, the height update equation for the height corresponding to location B is

$$H(i, j) = H(k, l) \pm m \sqrt{(l-j)^2 + (k-i)^2} \sqrt{N_r^2 + N_a^2}, \quad (60)$$

where the sign depends on the direction of the surface normal vector N and m is a normalization constant which determines the vertical scale. The sign is positive if the projection of the surface normal onto the lattice plane points away from the site (k, l) and toward the site (i, j) . If this is not the case, then the sign is negative. The two signs respectively correspond to ascending and descending slopes. We calculate the height for all the locations which fulfill the condition given in (53) for a chosen distance threshold f by considering only one reference height at the time. At the next iteration, we increase the maximal distance threshold f from (52), thus allowing us to update the height at additional sites. The two steps of the algorithm are repeated until all sites are visited. As we progressively increase f , we will find height estimates for an increasing number of sites. The maximal value for this threshold distance is $f = 1$. After evaluating the heights at all sites in the image, we calculate the local surface normals from



(a)



(b)

Fig. 11. The SAR gradient image when employing two different edge detectors. (a) Optimal edge detector for the Rayleigh-Bessel distribution. (b) Ratio-of-Averages edge detector.

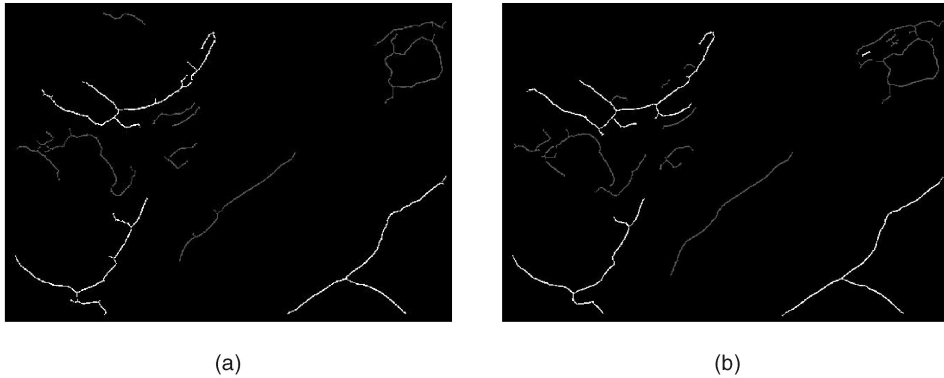


Fig. 12. Edge classification in a SAR image. (a) Edge classification when employing the optimal edge detector for the Rayleigh-Bessel distribution. (b) Edge classification when employing the ratio-of-averages edge detector.

the local height differences on r and a directions and compare them to the surface normals from the original vector field. The heights and the surface normals are iteratively updated by passing successively through the data until we achieve their consistency. The entire shape-from-shading method for SAR images is described in the diagram from Fig. 8. The first stage consists of solving low-level image processing problems such as nonlinear Lambertian correction and estimating edge features from radar image statistics. The SAR image statistics and the edge features are used in a shape-from-shading framework in which we model fields of surface normals. Eventually, the surface normals are used for calculating the 3D height information finalizing the mapping of a single SAR image of terrain into its corresponding 3D topography.

6 EXPERIMENTAL RESULTS

We have applied the proposed algorithm for radar shape-from-shading to SAR images of mountainous terrain captured from an aircraft. Fig. 3a shows a representative SAR image. Fig. 9 shows the amplitude distribution for a 100×100 pixel region selected from this image. Superimposed on the image data distribution are the estimated Rayleigh-Bessel (7) and

Rayleigh distributions. The Kolmogorov-Smirnov distance (10) of the fitted distribution is $D = 0.0447$ for the Rayleigh-Bessel and $D = 0.1166$ for Rayleigh. We have split the image into blocks and estimated the ratio $\hat{\nu}/\hat{\sigma}$. The resulting histogram of this ratio for the entire image is shown in Fig. 10. The Rayleigh distribution has the property that $\nu/\sigma = 1$. However, only a small percentage of data is located around this value, as we can see in Fig. 10. These results suggest that the Rayleigh-Bessel distribution is more appropriate than the Rayleigh distribution for SAR images of terrain.

In order to recover terrain shape from the given SAR image, we apply the maximum a posteriori model described in Section 2. First, we estimate the probability density function corresponding to edges, provided in (27). We detect the edges using the algorithm described in Section 4. The gradient image obtained when using the optimal estimator for the Rayleigh-Bessel distribution (31) is shown in Fig. 11a. For comparison, Fig. 11b shows the gradient when the ratio-of-averages algorithm is used instead [28], [29]. In both cases, we have used a 31×31 pixel window. The gradients obtained with the optimal edge detector for the Rayleigh-Bessel distribution are sharper and clearer than those detected by the ratio-of-averages estimator. The edges labeled as ridges and ravines using the classifier defined in (32) are shown in Fig. 12a. Fig. 12b displays the corresponding result obtained with the ratio-of-averages edge detector. The ridges are shown in a lighter gray-level, while the ravines are in a darker gray-level. From these figures, we can identify the main terrain features of the SAR image from Fig. 3a.

After applying the inverse reflectivity function derived in Section 3.3 and plotted in Fig. 4a, we obtain the image from Fig. 4c. We segment this image into blocks of size 20×20 and we estimate the parameters of the Rayleigh-Bessel distribution (7). The interference parameter denoted by μ is used to identify the regions covered by water and the back-slopes of mountains. We compute the apex angle of the reflection cone using the locally estimated mode of the Rayleigh-Bessel distribution. The edge map represented in Fig. 12a is used as a constraint in the recovery of the vector field of surface normals. The maximization of the local a posteriori surface normal probabilities $p(\mathcal{V}_j | \mathcal{E}_j, I_{2D})$ as described in Section 5.1, provides the vector field shown in Fig. 14a. From this needle map, it is clear that the ravines and ridges are estimated as centers of convergent and divergent vector fields of surface normals.

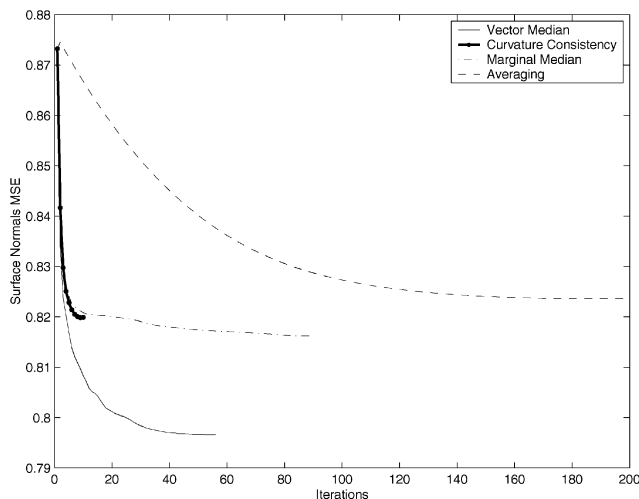


Fig. 13. Convergence in mean square error of the algorithms used for smoothing the surface normals.

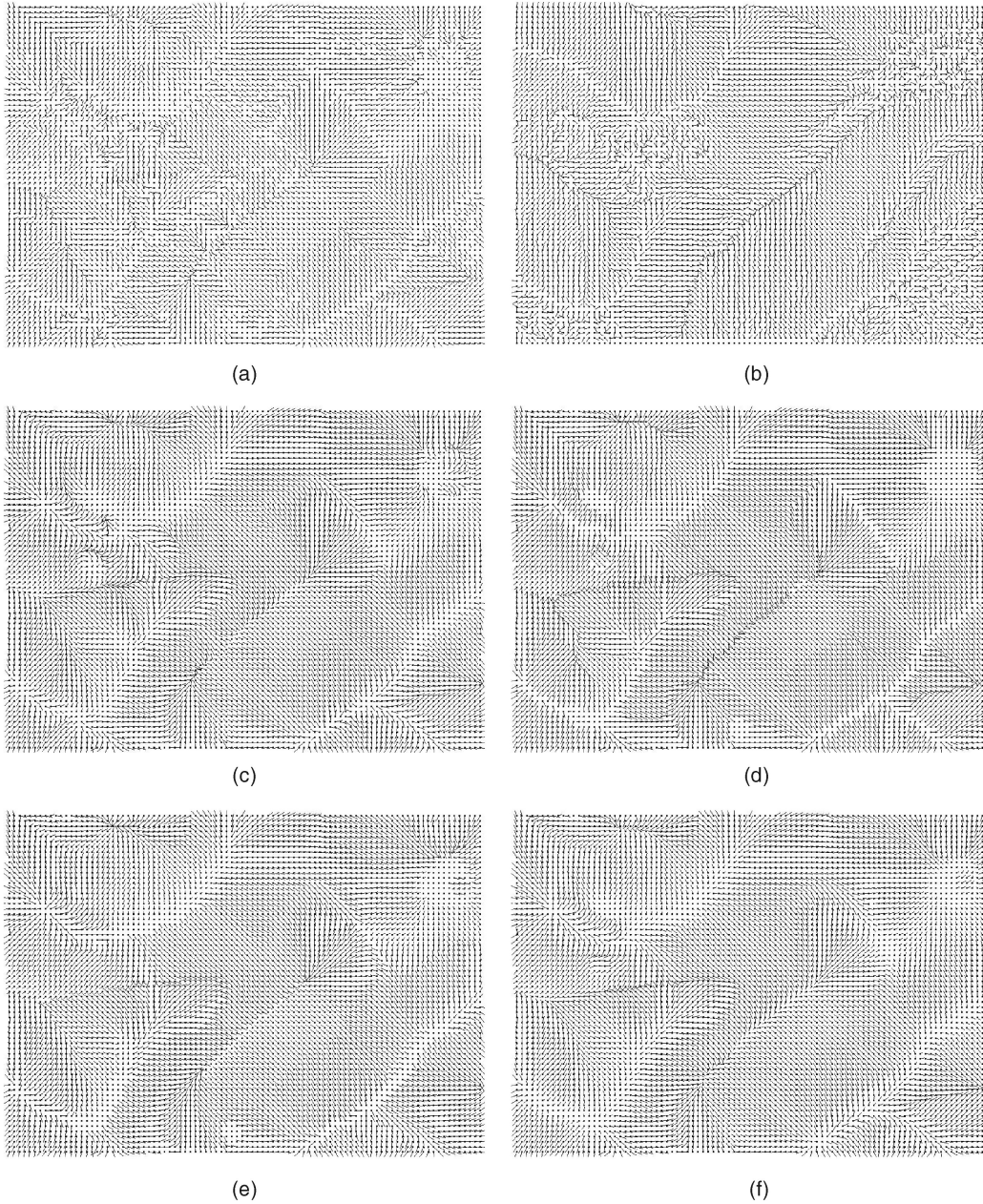


Fig. 14. Shape-from-shading in a SAR image of terrain. (a) Needle map initialization, (b) normal vector field of the digital elevation map. Needle-map smoothing using: (c) averaging, (d) marginal median, (e) vector median, and (f) curvature consistency.

We employ the iterative algorithm described in Section 5.2, for smoothing the vector field. This iterative updating involves two stages. In the first stage, each vector normal is modified toward an estimate of its neighbor vectors while maintaining the constraints imposed by the image statistics and by the reflectance function (36). In the second stage, the consistency of the updated surface normal with the local variance is verified according to (35). If a vector has its corresponding cone apex angle γ located outside the range provided by the local SAR image statistics, its value is corrected accordingly. The iterative updating algorithm of the surface normals continues until convergence is achieved.

The vector field obtained after averaging according to (42) is shown in Fig. 14c, while the vector fields smoothed by employing the marginal median (43) and the vector median

(44) estimators are shown in Figs. 14d and 14e, respectively. Fig. 14f shows the result obtained when using the surface curvature consistency algorithm (45)–(49). For each case, the smoothing neighborhood is a matrix of 3×3 vectors ($R = 9$). It is clear from all these figures that the resulting vector fields are quite smooth. The vector field of surface normals corresponding to the digital elevation map represented in Fig. 3b is shown in Fig. 14b. For quantitative comparisons, we use this vector field as a reference. This vector field is not very smooth due to the inaccuracies in the phase unwrapping recovery employed for calculating the DEM image. We consider two error measures in order to estimate the accuracy of the proposed algorithms. The first one is the mean square error between the reference vector field, denoted as \mathbf{N} , and that of the smoothed vector field, $\hat{\mathbf{N}}$, and is given by:

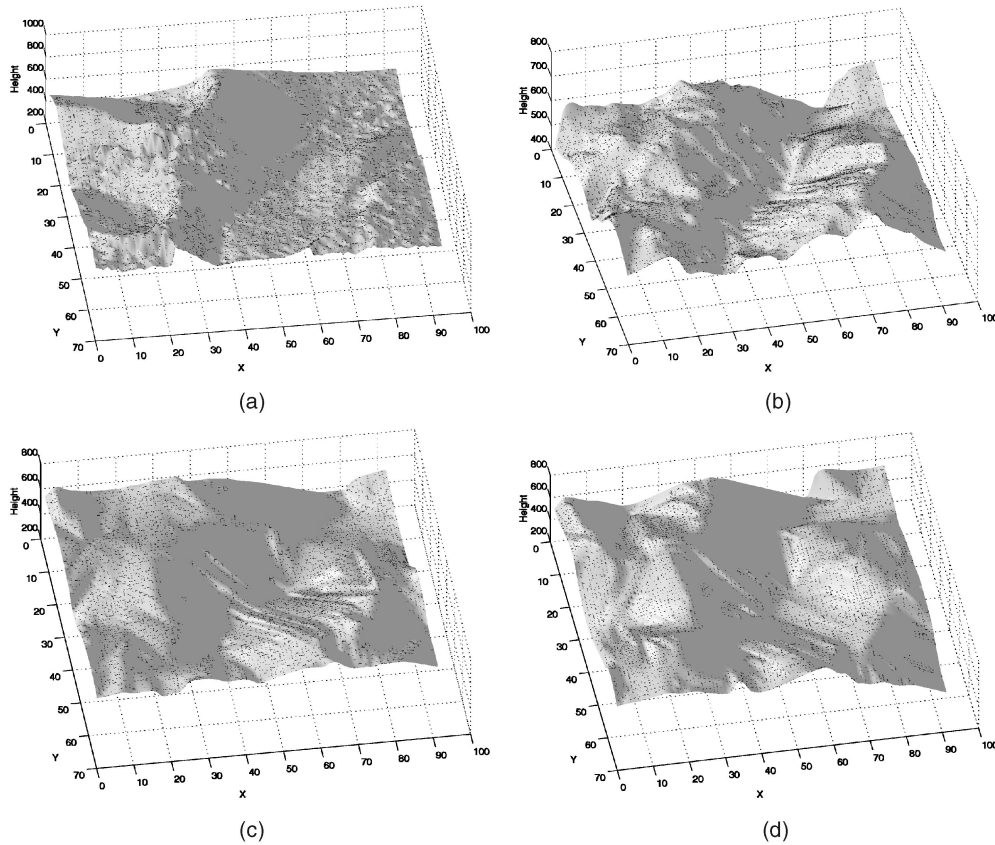


Fig. 15. Reconstructed 3D surfaces from the SAR image: (a) Original digital elevation map, (b) surface reconstructed from the surface normals before their smoothing, (c) using marginal median for smoothing surface normals, and (d) using vector median for smoothing surface normals.

$$MSE = \frac{1}{MP} \sum_{x=1}^M \sum_{y=1}^P \| \mathbf{N}_{(x,y)} - \hat{\mathbf{N}}_{(x,y)} \|, \quad (61)$$

where $\mathbf{N}_{(x,y)}$ denotes the vector located at the site (x, y) . The second error measure is the average cosine between the two vector fields:

$$MCE = \frac{1}{MP} \sum_{x=1}^M \sum_{y=1}^P \mathbf{N}_{(x,y)} \cdot \hat{\mathbf{N}}_{(x,y)}. \quad (62)$$

For the initial vector field of surface normals before applying any smoothing, we obtain $MSE = 0.873$ and $MCE = 0.606$ when considering as reference the vector field of the DEM. The convergence of surface field smoothing algorithms with respect to MSE is shown in Fig. 13.

Finally, we present some results to illustrate the surface reconstructions that can be obtained from smoothed needle-maps delivered by our shape-from-shading method. In Figs. 15 and 16, we compare the reconstructed surfaces with the ground truth provided by the digital elevation map. In the digital elevation map shown in Fig. 15a, there are a number of clear topographic features. First, there is a semicircular ridge in the top lefthand corner. Midway along the ridge, there is a rill which descends and meets with a ridge just below the main peak. There is also a deep valley which cuts across the plot at about 45 degrees and ends in the top righthand corner. The reconstructed maps are scaled to fit the range of heights for the DEM. In Fig. 15b, we show the surface reconstructed from the initial needle-map directions as they are derived from the statistics of the SAR image. Here, the valley emerges clearly, but the semicircular ridge and the rill are not well-defined. In

Figs. 15c and 15d, we show the surfaces obtained from the needle-maps delivered by marginal median smoothing and vector median smoothing. In both cases, the semicircular ridge and the rill are reconstructed. However, in the case of vector-median smoothing, the valley structure is badly disturbed. In Fig. 16, we provide a comparison with the results obtained with alternative algorithms. Fig. 16a shows the result obtained with the robust smoothing method of Worthington and Hancock [20]. Here, the semicircular ridge and the valley emerge well, but the rill is not detected. When vector averaging is applied to the initial needle-map, then the valley is well located, but the other features are oversmoothed, as can be seen in Fig. 16b. In Figs. 16c and 16d, we respectively compare with the Bichsel and Pentland [44] and Zheng and Chellappa algorithms [27]. These two algorithms compared favorably with other shape-from-shading algorithms in the survey from [23]. In order to use these SFS algorithms, we have processed the SAR image as in [11]. The Bichsel and Pentland method locates the semi-circular ridge, but exaggerates its height and introduces a large number of noisy peaks in the proximity of the valley. Some of the topographic features are just discernible in the output of the Zhang and Chellappa algorithm and the height is underestimated.

In Table 1, we provide numerical results for MSE and MCE for the surface normal fields, the average height error in the 3D surface reconstruction, as well as the number of iterations needed for convergence when smoothing the vector field of surface normals. From this table, we can see that the robust algorithms perform better than the classical approach of local vector averaging of the surface normals. Also, the number of iterations is much lower for the robust estimators. If the

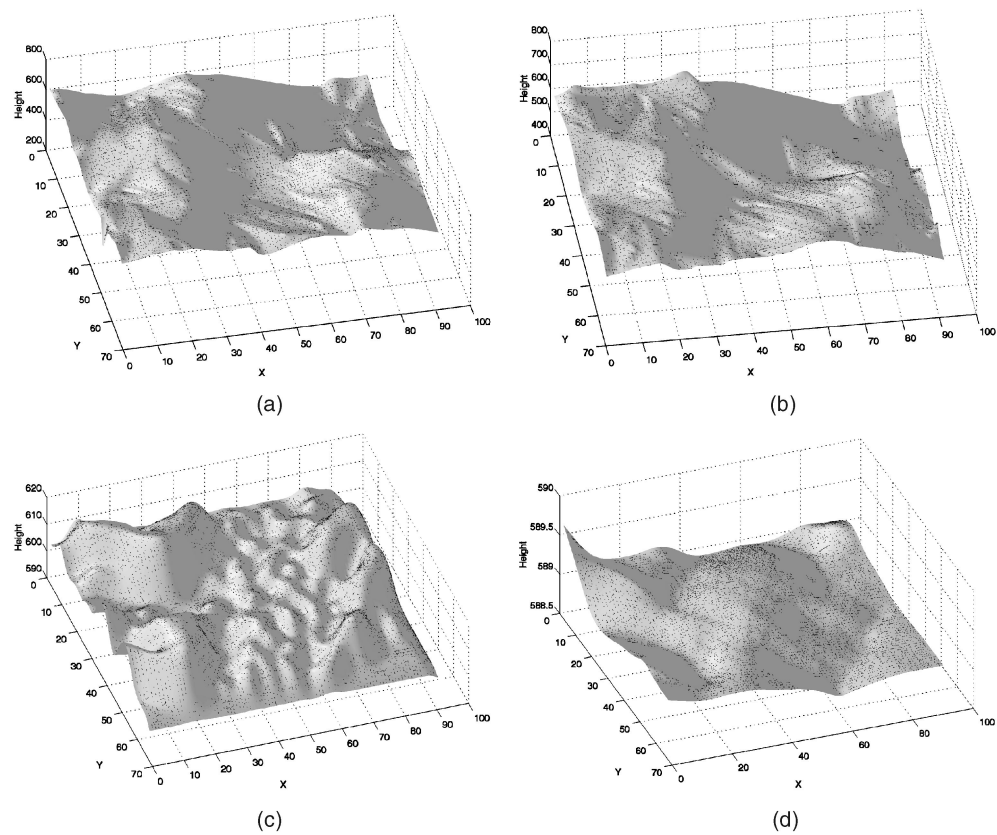


Fig. 16. Reconstructed 3D surfaces from the SAR image: (a) Using surface consistency smoothing for surface normals, (b) using averaging of surface normals, (c) surface generated using Bichsel and Pentland shape-from-shading, and (d) surface generated using Zheng and Chellappa shape from shading reconstruction algorithm.

estimated and ground truth reference surface normals have the same orientation, then the cosine of their angle difference would be 1. For comparison, we consider the algorithms of Bichsel and Pentland [44] and Zheng and Chellappa [27].

In Fig. 17, we show results obtained for radar images of Ayers Rock (mountain Uluru) and a neighboring region of mountainous topography. In Figs. 17a and 17b, we show the SAR images. Figs. 17c and 17d display the smoothed needle maps, while Figs. 17e and 17f show the reconstructed surface height data. In the case of the image from Fig. 17a, which shows Ayers Rock, the lower lefthand edge of the structure is well-reconstructed in both the needle-map and the height data. While the conditions of SAR image acquisition may be different for these images, we have considered the same reflectivity function as that modeled by (26). Unfortunately, the shading process fails in the shadow regions in the upper part of the image. Significant regions of shadowing or layover can pose problems to the proposed technique. In the case of the image from Fig. 17b, which shows a series of ridges, the overall structure is detected, but the fine detail is not reconstructed well.

7 CONCLUSIONS

This paper proposes a new approach for terrain reconstruction from SAR images using shape-from-shading. We embed the SFS approach in a maximum a posteriori framework. The novelty of the proposed approach consists of the way that various techniques are combined in order to solve the problems posed by terrain reconstruction from SAR images.

The main components of the proposed probabilistic model are: 1) the irradiance equation, 2) surface smoothing, and 3) the edge map topography constraint. We showed that the

TABLE 1
Comparison among Various Surface Normal Smoothing Algorithms when Reconstructing 3D Heights from SAR Images

Algorithm	MSE	MCE	Average Height Error	No. Iterations
Averaging	0.824	0.641	53.12	199
Marginal Median	0.816	0.644	45.19	88
Vector Median	0.797	0.658	50.43	55
Curvature Consistency	0.821	0.642	46.96	6
Zheng and Chellappa	1.306	0.174	84.32	500
Bichsel and Pentland	1.302	0.149	83.59	2

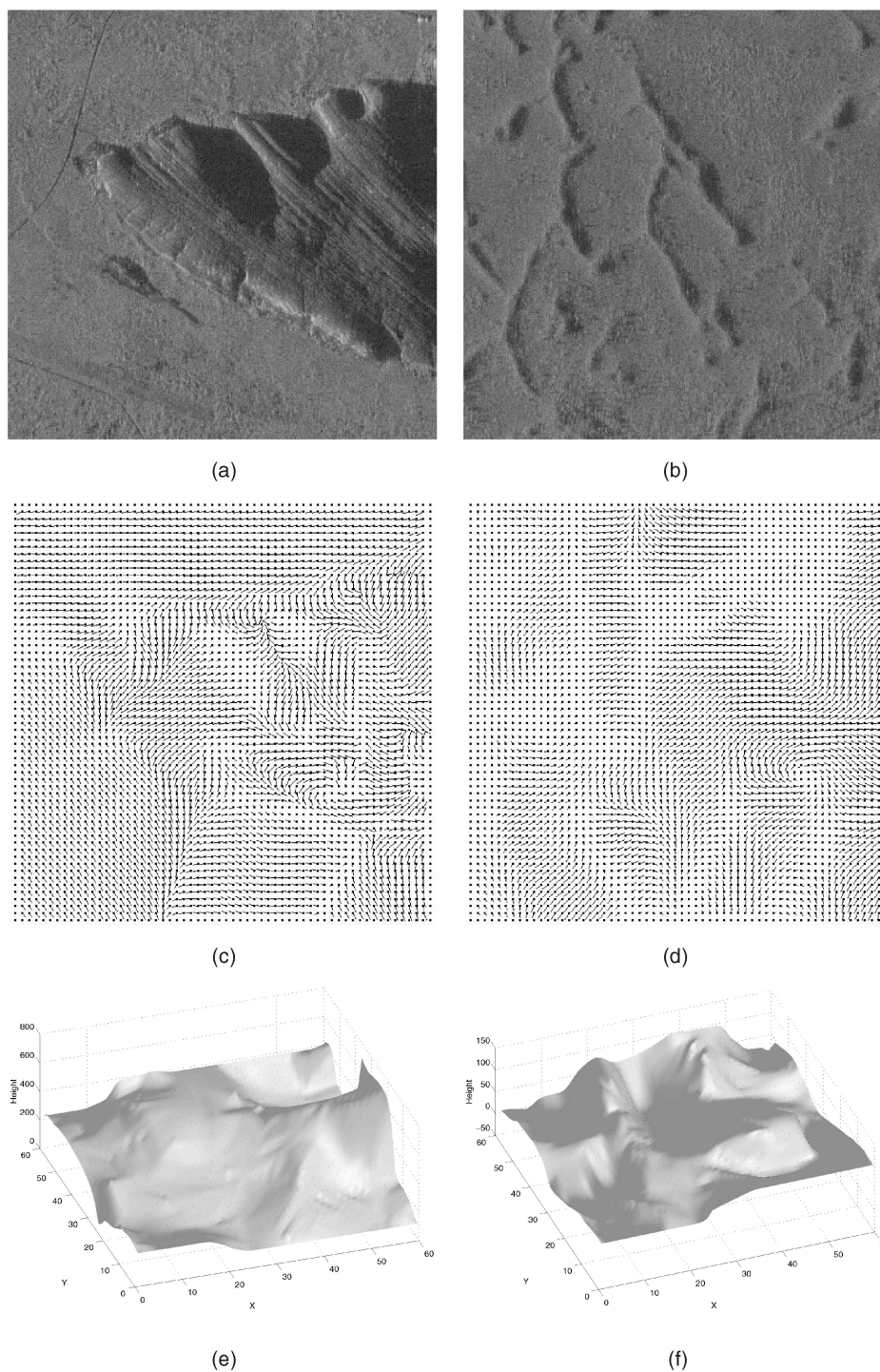


Fig. 17. Surface reconstruction from a region near Ayers Rock (Mount Uluru) in Australia: (a) SAR image of Ayers Rock, (b) topographical formations from Australia, (c) smoothed surface normals of Fig. 17a using curvature consistency, (d) smoothed surface normals extracted from Fig. 17b using vector median, and (e) and (f) height information derived from the surface normals.

characteristic distribution in SAR images is a product between the Rayleigh and Bessel functions. The parameters of this distribution are estimated using robust statistics. We compute the characteristic reflectance function using ground truth data provided by the 3D digital elevation map associated with the SAR image. We derive the optimal edge detector for the Rayleigh-Bessel distribution. The edges are classified as ridges and ravines and are used as constraints for deriving the surface orientation. The initial needle map,

representing the local surface orientation, is derived from the SAR image irradiance equation. We employ four different approaches for surface normal vector field smoothing: local averaging, the marginal median, the vector median, and a surface curvature consistency algorithm. The latter three approaches prove to be the most robust and provide the best estimates for the surface orientation. We suggest an algorithm for recovering the height information from the vector field of smoothed surface normals. The surface normal field or the

3D height map can be used for identifying topographical regions and, thus, for terrain description. Due to the relative difficulty of acquiring SAR images with ground truth, the experiments have been performed on a relatively limited set of data.

REFERENCES

- [1] J. *Geophysical Research-Planets*, special Magellan Issue, vol. 97, nos. 8 and 10, Aug./Sept. 1992.
- [2] M.I. Skolnik, *Radar Handbook*. New York: McGraw-Hill, 1970.
- [3] F.T. Ulaby, R.K. Moore, and A.K. Fung, *Microwave Remote Sensing: Active and Passive, Microwave Remote Sensing Fundamentals and Radiometry*. vol. 1, Reading, Mass.: Addison-Wesley, 1981.
- [4] R.L. Wildey, "Topography from Single Radar Images," *Science*, vol. 224, no. 4645, pp. 153-156, 1984.
- [5] J. Thomas, W. Kober, and F. Leberl, "Multiple Image SAR Shape-from-Shading," *Photogrammetric Eng. and Remote Sensing*, vol. 57, no. 1, pp. 51-59, Jan. 1991.
- [6] T. Hagfors and W. Kofman, "Mapping of Overspread Targets in Radar Astronomy," *Radio Science*, vol. 26, no. 2, pp. 403-416, 1991.
- [7] T. Bayer, R. Winter, and G. Schreier, "Terrain Influences in SAR Backscatter and Attempts to Their Correction," *IEEE Trans. Geoscience and Remote Sensing*, vol. 29, no. 3, pp. 451-462, May 1991.
- [8] D.J. Goering, H. Chen, L.D. Hinzman, and D.L. Kane, "Removal of Terrain Effects from SAR Satellite Imagery of Arctic Tundra," *IEEE Trans. Geoscience and Remote Sensing*, vol. 33, no. 1, pp. 185-194, Jan. 1995.
- [9] W.G. Carrara, R.S. Goodman, and R.M. Majewski, *Spotlight Synthetic Aperture Radar Signal Processing Algorithms*. Artech House, 1995.
- [10] A.F.C. Haldemann and D.O. Muhleman, "Circular-Polarization Radar Properties of High-Altitude Ice: Western Kunlun Shan and Central Andes," *J. Geophysical Research—Planets*, vol. 104, no. E10, pp. 24075-24094, Oct. 1999.
- [11] R.T. Frankot and R. Chellappa, "Estimation of Surface Topography from SAR Imagery Using Shape from Shading Techniques," *Artificial Intelligence*, vol. 43, pp. 271-310, 1990.
- [12] B. Guindon, "Development of a Shape-from-Shading Technique for the Extraction of Topographic Models from Individual Spaceborn SAR Images," *IEEE Trans. Geoscience and Remote Sensing*, vol. 28, no. 4, pp. 654-661, July 1990.
- [13] P. Fua, "Fast, Accurate and Consistent Modeling of Drainage and Surrounding Terrain," *Int'l J. Computer Vision*, vol. 26, no. 3, pp. 215-234, 1998.
- [14] R. Bolter and A. Pinz, "3D Exploitation of SAR Images," *Proc. Machine Vision and Advanced Image Processing in Remote Sensing Workshop*, pp. 160-169, May 1998.
- [15] R. Caves, S. Quegan, and R. White, "Quantitative Comparison of the Performance of SAR Segmentation Algorithms," *IEEE Trans. Image Processing*, vol. 7, no. 11, pp. 1534-1546, Nov. 1998.
- [16] D.N. Ostrov, "Boundary Conditions and Fast Algorithms for Surface Reconstructions from Synthetic Aperture Radar Data," *IEEE Trans. Geoscience and Remote Sensing*, vol. 37, no. 1, pp. 335-346, Jan. 1999.
- [17] A.G. Bors, E.R. Hancock, and R.C. Wilson, "A Bayesian Framework for Radar Shape-from-Shading," *Proc. IEEE Conf. Computer Vision and Pattern Recognition*, vol. 1, pp. 262-268, June 2000.
- [18] K. Ikeuchi and B.K.P. Horn, "Numerical Shape from Shading and Occluding Boundaries," *Artificial Intelligence*, vol. 17, pp. 141-184, 1981.
- [19] B.K.P. Horn and M.J. Brooks, "The Variational Approach to Shape from Shading," *Computer Vision, Graphics, Image Processing*, vol. 33, no. 2, pp. 174-208, 1986.
- [20] P.L. Worthington and E.R. Hancock, "New Constraints on Data-Closeness and Needle Map Consistency for Shape-from-Shading," *IEEE Trans. Pattern Analysis and Machine Intelligence*, vol. 21, no. 12, pp. 1250-1267, Dec. 1999.
- [21] J. Oliensis and P. Dupuis, "An Optimal Control Formulation and Related Numerical Methods for a Problem in Shape Reconstruction," *Ann. Application Probability*, vol. 4, no. 2, pp. 287-346, 1994.
- [22] R. Kimmel and A.M. Bruckstein, "Tracking Level-Sets by Level-Sets: A Method for Solving the Shape from Shading Problem," *Computer Vision and Image Understanding*, vol. 62, no. 1, pp. 47-58, 1995.
- [23] R. Zhang, P.-S. Tsai, J.E. Cryer, and M. Shah, "Shape from Shading: A Survey," *IEEE Trans. Pattern Analysis and Machine Intelligence*, vol. 21, no. 8, pp. 690-706, Aug. 1999.
- [24] S. Paquereault, H. Maitre, and J.-M. Nicolas, "Radarclinometry for ERS-1 Data Mapping," *Proc. IEEE Int'l Geoscience and Remote Sensing Symp.*, vol. 1, pp. 503-505, Apr. 1996.
- [25] J. Chorowicz, T. Rouis, J.-P. Rudant, and S. Manoussis, "Computer Aided Recognition of Relief Patterns on Radar Images Using a Syntax Analysis," *Remote Sens. Environ.*, vol. 64, pp. 221-233, 1998.
- [26] R. Kimmel, K. Siddiqi, B.B. Kimia, and A.M. Bruckstein, "Shape-from-Shading—Level Set Propagation and Viscosity Solutions," *Int'l J. Computer Vision*, vol. 16, no. 2, pp. 107-133, 1995.
- [27] Q. Zheng and R. Chellappa, "Estimation of Illuminant Direction, Albedo, and Shape from Shading," *IEEE Trans. Pattern Analysis and Machine Intelligence*, vol. 13, no. 7, pp. 680-702, July 1991.
- [28] A.C. Bovik, "On Detecting Edges in Speckle Imagery," *IEEE Trans. Acoustics, Speech, and Signal Processing*, vol. 36, no. 10, pp. 1618-1627, Oct. 1988.
- [29] C.J. Oliver, D. Blacknell, and R.G. White, "Optimum Edge Detection in SAR," *IEE Proc.—Radar, Sonar, Navigation*, vol. 143, no. 1, pp. 31-40, Feb. 1996.
- [30] R. Fjortoft, P. Marthon, A. Lopes, and E. Cubero-Castan, "Multi-edge Detection in SAR Images," *Proc. IEEE Int'l Conf. Acoust. Speech and Sig. Proc.*, vol. 4, pp. 2761-2764, Apr. 1997.
- [31] R.R. Zito, "The Shape of SAR Histograms," *Computer Vision, Graphics, and Image Processing*, vol. 43, pp. 281-293, 1988.
- [32] R. Bolter, M. Gelautz, and F. Leberl, "SAR Speckle Simulation," *Int'l Archives of Photogrammetry and Remote Sensing*, vol. 21, pp. 20-25, 1996.
- [33] A.N. Evans, N.G. Sharp, and E.R. Hancock, "Noise Models for Linear Feature Detection in SAR Images," *Proc. IEEE Int'l Conf. Image Processing*, vol. 1, pp. 466-470, Nov. 1994.
- [34] R. Touzi, A. Lopes, and P. Bousquet, "A Statistical and Geometrical Edge Detector for SAR Images," *IEEE Trans. Geoscience and Remote Sensing*, vol. 26, no. 6, pp. 764-773, Nov. 1988.
- [35] M. Beauchemin, K.P.B. Thomson, and G. Edwards, "On Nonparametric Edge Detection in Multilook SAR Images," *IEEE Trans. Geoscience and Remote Sensing*, vol. 36, no. 5, pp. 1826-1829, Sept. 1998.
- [36] R.N. Czerwinski, D.L. Jones, and W.D. O'Brien Jr., "Line and Boundary Detection in Speckle Images," *IEEE Trans. Image Processing*, vol. 7, no. 12, pp. 1700-1713, Dec. 1998.
- [37] M. Datcu, K. Seidel, and M. Walessa, "Spatial Information Retrieval from Remote-Sensing Images—Part I: Information Theoretical Perspective," *IEEE Trans. Geoscience and Remote Sensing*, vol. 36, no. 5, pp. 1431-1445, Sept. 1998.
- [38] S. Geman and D. Geman, "Stochastic Relaxation, Gibbs Distributions, and the Bayesian Restoration of Images," *IEEE Trans. Pattern Analysis and Machine Intelligence*, vol. 6, no. 6, pp. 721-741, Nov. 1984.
- [39] G. Seber, *Multivariate Observations*. New York: John Wiley, 1986.
- [40] I. Pitas and A.N. Venetsanopoulos, *Nonlinear Digital Filters: Principles and Applications*. Norwell, Mass.: Kluwer Academic, 1990.
- [41] A.G. Bors and I. Pitas, "Median Radial Basis Function Neural Network," *IEEE Trans. Neural Networks*, vol. 7, no. 6, pp. 1351-1364, Nov. 1996.
- [42] J. Astola, P. Haavisto, and Y. Neuvo, "Vector Median Filters," *Proc. IEEE*, vol. 78, no. 4, pp. 678-689, 1990.
- [43] A.G. Bors and E.R. Hancock, "Recovering Height Information from SAR Images of Terrain," *Proc. IEEE Int'l Conf. Image Processing*, vol. 2, pp. 477-480, Sept. 2002.
- [44] M. Bichsel and A. Pentland, "A Simple Algorithm for Shape from Shading," *Proc. IEEE Computer Vision and Pattern Recognition*, pp. 459-465, 1992.
- [45] J.R.A. Torrealo, "Bayesian Shape Estimation: Shape-from-Shading and Photometric Stereo Revisited," *Machine Vision and Applications*, vol. 8, pp. 163-172, 1995.
- [46] R.C. Wilson and E.R. Hancock, "Bias-Variance Analysis for Controlling Adaptive Surface Meshes," *Computer Vision and Image Understanding*, vol. 77, pp. 25-47, Jan. 2000.
- [47] G. Lohman, *Volumetric Image Analysis*. J. Wiley-Teubner, 1998.
- [48] A. Papoulis, *Probability, Random Variables and Stochastic Processes*. second ed., McGraw-Hill, 1984.
- [49] M. Abramowitz and I.A. Stegun, *Handbook of Math. Functions*. New York: Dover, 1972.
- [50] W.H. Press, S.A. Teukolsky, W.T. Vetterling, and B.P. Flannery, *Numerical Recipes in C*. second ed., Cambridge Univ. Press, 1992.
- [51] P. Huber, *Robust Statistics*. Wiley, 1981.

- [52] D.C. Ghilgia and M.D. Pitt, *Two-Dimensional Phase Unwrapping: Theory, Algorithms, and Software*. New York: John Wiley, 1998.
- [53] *Markov Random Fields: Theory and Application*. R. Chellappa and A.K. Jain, eds. Academic Press, 1993.
- [54] E.R. Hancock and J. Kittler, "Adaptive Estimation of Hysteresis Thresholds," *Proc. IEEE Conf. Computer Vision and Pattern Recognition*, pp. 196-201, June 1991.
- [55] A. Lopes, E. Nezry, R. Touzi, and H. Laur, "Structure Detection and Statistical Adaptive Speckle Filtering in SAR Images," *Int'l J. Remote Sensing*, vol. 14, no. 9, pp. 1735-1758, 1993.
- [56] S.A. Kassam, *Signal Detection in Non-Gaussian Noise*. Springer-Verlag, 1988.
- [57] J. Sera, *Image Analysis and Math. Morphology*. New York: Academic Press, 1982.
- [58] J.J. Koenderink and A.J. van Doorn, "Surface Shape and Curvature Scales," *Image and Vision Computing*, vol. 10, pp. 557-565, 1992.



Adrian G. Bors received the MS degree in electronics engineering from the Polytechnic University of Bucharest, Romania, in 1992 and the PhD degree in informatics from the University of Thessaloniki, Greece, in 1999. From September 1992 to August 1993, he was a research scientist at the Signal Processing Laboratory, Tampere University of Technology, Finland. From 1993 to 1999, he was a research associate, first with the Department of Electrical

and Computer Engineering and, afterward, with the Department of Informatics at the University of Thessaloniki. During this period, he contributed to various European research projects. In March 1999, he joined the Department of Computer Science, University of York, United Kingdom, as a postdoctoral research associate, where he is currently a lecturer. Dr. Bors has been an associate editor of the *IEEE Transactions on Neural Networks* since 2001, and was a member of the organizing committee for the IEEE International Conference on Image Processing 2001. He has published more than 50 papers in journals, edited books, and international conferences. His research interests include computer vision, image processing, neural networks, pattern recognition, and nonlinear digital signal processing. He is a member of the IEEE and the IEEE Computer Society.



Edwin R. Hancock studied physics as an undergraduate at the University of Durham and graduated with honors in 1977. He remained at Durham to complete the PhD degree in the area of high energy physics in 1981. Following this, he worked for 10 years as a researcher in the fields of high-energy nuclear physics and pattern recognition at the Rutherford-Appleton Laboratory (now the Central Research Laboratory of the Research Councils). During this period, he

also held adjunct teaching posts at the University of Surrey and the Open University. In 1991, he moved to the University of York as a lecturer in the Department of Computer Science. He was promoted to senior lecturer in 1997 and to reader in 1998. In 1998, he was appointed to a chair in computer vision. Professor Hancock now leads a group of some 18 faculty, research staff, and PhD students working in the areas of computer vision and pattern recognition. His main research interests are in the use of optimization and probabilistic methods for high and intermediate level vision. He is also interested in the methodology of structural and statistical pattern recognition. He is currently working on graph-matching, shape-from-X, image data bases, and statistical learning theory. His work has found applications in areas such as radar terrain analysis, seismic section analysis, remote sensing, and medical imaging. He has published some 75 journal papers and 250 refereed conference publications. He was awarded the Pattern Recognition Society medal in 1991 for the best paper to be published in the journal *Pattern Recognition*. The journal also awarded him an outstanding paper award in 1997. He has been a member of the editorial boards of the journals *IEEE Transactions on Pattern Analysis and Machine Intelligence* and *Pattern Recognition*. He has also been a guest editor for special editions of the journals *Image and Vision Computing* and *Pattern Recognition*, and he is currently a guest editor of a special edition of *IEEE Transactions on Pattern Analysis and Machine Intelligence* devoted to energy minimization methods in computer vision. He has been on the program committees for numerous national and international meetings. In 1997, he coestablished a new series of international meetings on energy minimization methods in computer vision and pattern recognition. In 2000, he became a fellow of the IAPR.



Richard C. Wilson received the BA degree in physics from the University of Oxford in 1992. In 1996, he received the DPhil degree from the University of York for his thesis "Inexact Graph Matching Using Symbolic Constraints." From 1996 to 1998, he worked as a research associate at the University of York. After a period of postdoctoral research, he was awarded an Advanced Research Fellowship in 1998, a position which he currently holds in the

Department of Computer Science at the University of York. He has published some 70 papers in journals, edited books, and refereed conferences. He received an outstanding paper award in the 1997 Pattern Recognition Society awards and has won the best paper prize in ACCV 2002. He is currently an associate editor of the journal *Pattern Recognition*. His research interests are in statistical and structural pattern recognition, graph methods for computer vision, high-level vision, and scene understanding. He is a member of the IEEE Computer Society.

► For more information on this or any other computing topic, please visit our Digital Library at <http://computer.org/publications/dlib>.